P–T–X conditions on the genesis of orogenic Au (As, Bi, Ag) deposit in metasedimentary rocks of the Buracão Area, Araí Group, Brasília Fold Belt, Brazil

G.L.C. Pires[a,c,*], C. Renac[b], E.M. Bongiolo[c], R. Neumann[d], A. Barats[b]

[a] *Programa de Pós–graduação em Geologia – PPGL, Universidade Federal do Rio de Janeiro – UFRJ, CEP 21941-916 Rio de Janeiro, Brazil*
[b] *Université de Nice – Sophia Antipolis, GEOAZUR UMR 7329, FR 06560 Valbonne, France*
[c] *Instituto de Geociências, Universidade Federal do Rio de Janeiro – UFRJ, CEP 21941-916, Rio de Janeiro, Brazil*
[d] *Centro de Tecnologia Mineral – CETEM, Rio de Janeiro, Brazil*

ABSTRACT

The orogenic Au (As, Bi, Ag) mineralization (up to 31 g/t) of the Buracão area is hosted in the metasedimentary Paleo–Mesoproterozoic Traíras Formation, Araí Group, Brasília Fold Belt, Brazil. In order to discuss the P–T–X conditions that generated this mineralization, we present mineralogical, geochemical and fluid inclusion data of veins, gold and wall rocks. Coupled with previous structural data these additional data allow us to link metamorphism and deformation with fluid migration and ore genesis. The integration of fluid inclusion microthermometry with mineral geothermobarometers and structures show that rocks of the study area evolved from: (i) syn–D_{1a} metamorphic peak (400–560 °C, < 6 kbar), through to the (ii) development of syn–D_{1b} type I barren veins from low salinity H_2O–NaCl fluids during syn– to late–metamorphic peak; and to the (iii) development of syn–D_{2a} type II veins with the pyritic ore precipitation from low to high salinity H_2O–CO_2–CH_4–NaCl ± HCO_3 fluids during post–metamorphic peak (345–285 °C, 2.7–1.6 kbar).

The high fineness gold nuggets accompanied by As, Bi and Ag within pyrite–arsenopyrite–bismuthinite association in the pyritic ore allows the Buracão area to be classified as "a gold-only orogenic ore deposit". Fluid inclusion compounds and the enrichment of As, Bi, Pb, Cu, Te, Se and Ag in pyrite from the pyritic ore point out to metamorphism of carbonaceous phyllites and carbonate rocks of the Traíras Formation as a source for ore–forming fluids. We suggest that sulfur and gold in these fluids were derived by metamorphism of sedimentary rocks and conversion of pyrite into pyrrhotite in a metamorphic–hydrothermal system. The $Au(HS)_2^-$–bearing fluids percolated along intrabasinal D_{2a} regional shear zones through the Traíras Formation towards the Buracão area, where they precipitated type II ore–bearing veins within local structures. The ore precipitation was induced by contrasting fO_2–fS_2 related to the interaction between the sulfur-bearing fluid and host magnetite–graphite phyllites. The lithological control is represented by a series of reactions such as $2FeO_{(in\ silicates/magnetite)} + 4Au(HS)_{2(aq)}^- + 4H_{(aq)}^+ \leftrightarrow 2FeS_{2(s)} + 4Au_{(s)} + 4H_2S_{(aq)} + 2H_2O_{(l)}$.

The deposits of the Buracão area and other orogenic gold deposits hosted in metasedimentary rocks in the Brasília Fold Belt and worldwide confirm the potential of ore genesis in zones that do not show any relation with (meta)igneous rocks, thus, expanding the exploration possibilities in metasedimentary successions.

1. Introduction

In the last two decades, much has been discussed regarding the fluids responsible for orogenic gold deposits worldwide (e.g., Phillips and Powell, 1993; Groves et al., 1998). Recently, many authors have debated the participation of magmatic– versus metamorphic–hydrothermal fluids on the generation of these deposits (e.g., Tomkins, 2013; Doublier et al., 2014; Goldfarb and Groves, 2015). Even considering a metamorphic–hydrothermal source, another question concerns the potential for metaigneous and metasedimentary rocks to generate auriferous fluids, and also to control or influence ore precipitation (e.g., Goldfarb et al., 2005; Phillips and Powell, 2010). In this way, the understanding of orogenic gold deposits hosted solely within metasedimentary successions is the key to evaluate their typical
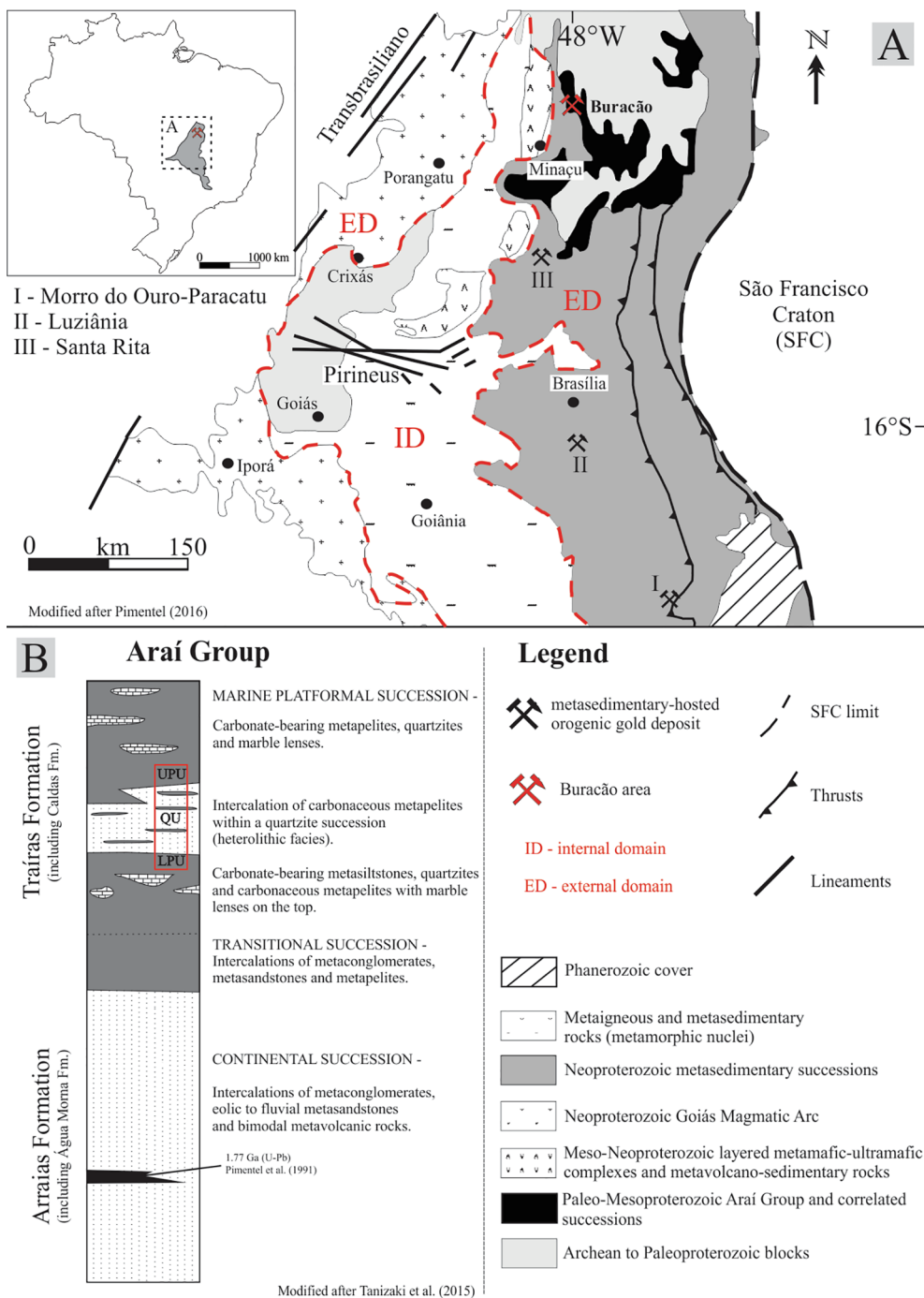
---

* Corresponding author.
  E-mail address: g.pires@geologia.ufrj.br (G.L.C. Pires).

Fig. 1. Regional geological setting with: (A) location of the Buracão area and other Neoproterozoic metasedimentary–hosted orogenic gold deposits in the external domain of the northern zone of the Neoproterozoic Brasília Fold Belt (insert: location of the Buracão area and Brasília Fold Belt in the Brazilian territory); and (B) stratigraphic position of the Buracão area (red rectangle) in the Traíras Formation, upper succession of the Paleo–Mesoproterozoic metasedimentary Araí Group. LPU: Low Phyllite Unit; QU: Quartzite Unit; UPU: Upper Phyllite Unit. (For interpretation of the references to color in this figure legend, the reader is referred to the web version of this article.)

geological and geochemical fingerprints (e.g., Pitcairn et al., 2006; Thomas et al., 2011). Several orogenic gold deposits have been reported within turbidite-, shallow platformal- and rift-related metamorphosed sedimentary successions from Archean to Phanerozoic ages worldwide. The deposits are structurally controlled both in vein and disseminated styles, usually associated with carbonaceous phyllites or black shales, where pyrite and arsenopyrite are the main sulfide ore (e.g., Large et al., 2011).

In Brazil, the northern zone of the Neoproterozoic Brasília Fold Belt (BFB; Fig. 1A) hosts small–scale to world–class orogenic gold deposits associated with low– to medium–grade metasedimentary successions (e.g., Dardenne and Botelho, 2014; Fig. 1A). These deposits contain gold in association with As–Ag–Bi–S, related to H_2O–CO_2–CH_4 (N_2) metamorphic fluids, and pressure (P) and temperature (T) conditions

for an ore deposition at 300 °C ± 75 and 1.5–3.0 kbar, as reported at Luziânia, Santa Rita and the world–class Morro do Ouro–Paracatu deposits (e.g., Hagemann et al., 1992; Giuliani et al., 1993; Oliver et al., 2015; Fig. 1A). Besides these localities, there are poorly studied gold occurrences hosted in the Paleo–Mesoproterozoic Araí Group, near to the Minaçu district, such as the Buracão area, the focus of this work (Fig. 1B). Gold mineralization in the Buracão area occurs in quartz veins, within a metamorphosed marine shelf succession (i.e., the upper Traíras Formation), located within a region without the occurrence of any syn–tectonic (meta)igneous rocks (cf. Pires et al., 2016).

The present work aims to investigate the P–T–X conditions on the genesis of orogenic Au (As, Bi, Ag) mineralization and its relation with the low–grade metamorphism of the sedimentary succession of the Traíras Formation in the Buracão area. This study presents

mineralogical, geochemical and fluid inclusion data from veins, gold and wall–rocks that coupled with previous structural data permit an interpretation of the geological processes related to sources of metals and fluid, their transport and the deposition of gold ore.

2. Geological setting

The N–S–trending Brasília Fold Belt (BFB) comprises a metamorphic nucleus and an external fold–and–thrust belt. It records a metamorphic peak between 650 and 630 Ma, associated with the Brasiliano–Pan African Orogeny, as part of the Western Gondwana assembly (e.g., Pimentel, 2016). The BFB comprises a series of Archean to Paleoproterozoic blocks, Paleo–Mesoproterozoic metasedimentary successions (e.g., Araí Group and correlated Serra da Mesa and Natividade groups) and younger layered metamafic–metaultramafic complexes associated with metavolcano–sedimentary rocks. The Neoproterozoic pre– to syn–collisional rocks comprise the arc–related metaigneous and metasedimentary rocks as well as a platformal siliciclastic succession with carbonate rocks (e.g., Pimentel et al., 2000; Dardenne, 2000; Pimentel, 2016 and references therein; Fig. 1A).

The metasedimentary succession of the Araí Group was originally deposited in a Paleo–Mesoproterozoic rift basin, and then metamorphosed and deformed during the Neoproterozoic Brasiliano–Pan African Orogeny (e.g., Dardenne, 2000; Fig. 1B). This Group is interpreted as (i) a continental succession – the basal Arraias Formation – composed of eolian to fluvial metasandstones and metaconglomerates, with locally bimodal metavolcanic rocks (1.77 Ga; Pimentel et al., 1991); and (ii) the upper Traíras Formation represented by a 575-m-thick phyllite–quartzite–marble succession interpreted originally as records of a transitional continental– and shelf–marine siliciclastic–carbonate succession (e.g., Dardenne et al., 2000; Tanizaki et al., 2015; Fig. 1B).

A geological summary of the Buracão area (cf. Pires et al., 2016) is presented here as background information. It is located in the external domain of the BFB and comprises (i) two phyllite units (Lower–LPU and Upper–UPU); and (ii) an intermediate Quartzite Unit (QU) with intercalations of phyllite lenses, all associated with the upper Traíras Formation of the Araí Group (Fig. 1B). These rocks record greenschist facies metamorphism (biotite zone, 425–500 °C) and two deformational phases, each subdivided in two stages (D_{1a} and D_{1b}/D_{2a} and D_{2b}; Table 1).

The quartz vein systems comprise barren type I and ore–bearing type II veins (Table 1). Barren veins (Fig. 2A and B; Table 1) are associated with fold–related, conjugated shear fractures developed during D_{1b} folding of competent quartzite beds. Ore–bearing veins (Fig. 2C to F; Table 1; up to 31 g/t Au; Paringa Resources, 2012) are associated with a Riedel shear fracture system related to subvertical NNE–trending High Deformation Zones (see Fig. 9 of Pires et al., 2016), regionally associated with crustal–scale shear zones. The type II ore–bearing veins are syn–D_{2a} deformational stage, and therefore, were formed after syn–D_{1b} type I barren veins. Besides structural controls, type II ore–bearing veins are closely associated with phyllite lenses intercalated within the Quartzite Unit (QU; Fig. 2F).

3. Methods

3.1. Sampling and mineral preparations

The present paper is based on the study of nineteen artisanal minings (*garimpos*) located in the Quartzite Unit (QU; see Fig. 7 of Pires et al., 2016), where both barren and ore–bearing veins, unaltered and hydrothermally altered host rocks were described and sampled. Panning of the collected material allowed the concentration of trace and heavy minerals/gold grains from vein samples. Further mineral separations used techniques including an isodynamic electromagnetic separator, dense liquids and hand–picking of grains under binoculars.

3.2. Optical and scanning electron microscopy (SEM–EDS)

Minerals were identified by reflected light microscopy and a FEI Quanta 400 Scanning Electron Microscopy (SEM) equipped with Energy Dispersive X-ray Fluorescence Spectroscopy detector (EDS) at Centro de Tecnologia Mineral (CETEM/RJ). The SEM was coupled to a Bruker Quantax 800 system with an XFlash and a silicon drift detector combined with calibrated lab standards (i.e., pyrite, hematite, Mn–oxides and Cu–Mn–metals) that allowed a semi–quantitative estimation of major elements proportions in weight (wt. %) and atomic (at. %) percentages. Results were used to estimate structural formulae of sulfides. The Au and Ag relative contents of 91 gold grains from thirteen type II ore–bearing veins were used to calculate the fineness values (Fn = [100·Au/(Au + Ag)]; Morrison et al., 1991) and perform qualitative comparisons.

3.3. X–ray crystallography

Mineral identification of hydrothermally altered and unaltered phyllites (i.e., seven samples from the LPU and QU), as well as separates of white mica (five samples from barren and ore veins), pyrite and pyrrhotite (six and one samples from pyritic ore, respectively) were completed by X–ray diffraction (XRD). A Bruker-D4 Endeavor diffractometer was used; Co $K_{\alpha1+2}$, 40 kV, 40 mA equipped with a LynxEye detector 250 s/1° 2θ. X-ray diffractograms of phyllite (whole–rock) as well as white mica were conducted in random powder and oriented (air–dried, ethylene–glycol solvated, and heat–treated) preparations, and included a comparative crystallinity index (Full Width at Half Maximum intensity – FWHM) and polytype identification (cf. Zviagina et al., 2007). White mica and sulfide separates were characterized by random powder preparations in order to certify their purity and minimize the influence of mineral inclusions in chemical analyses.

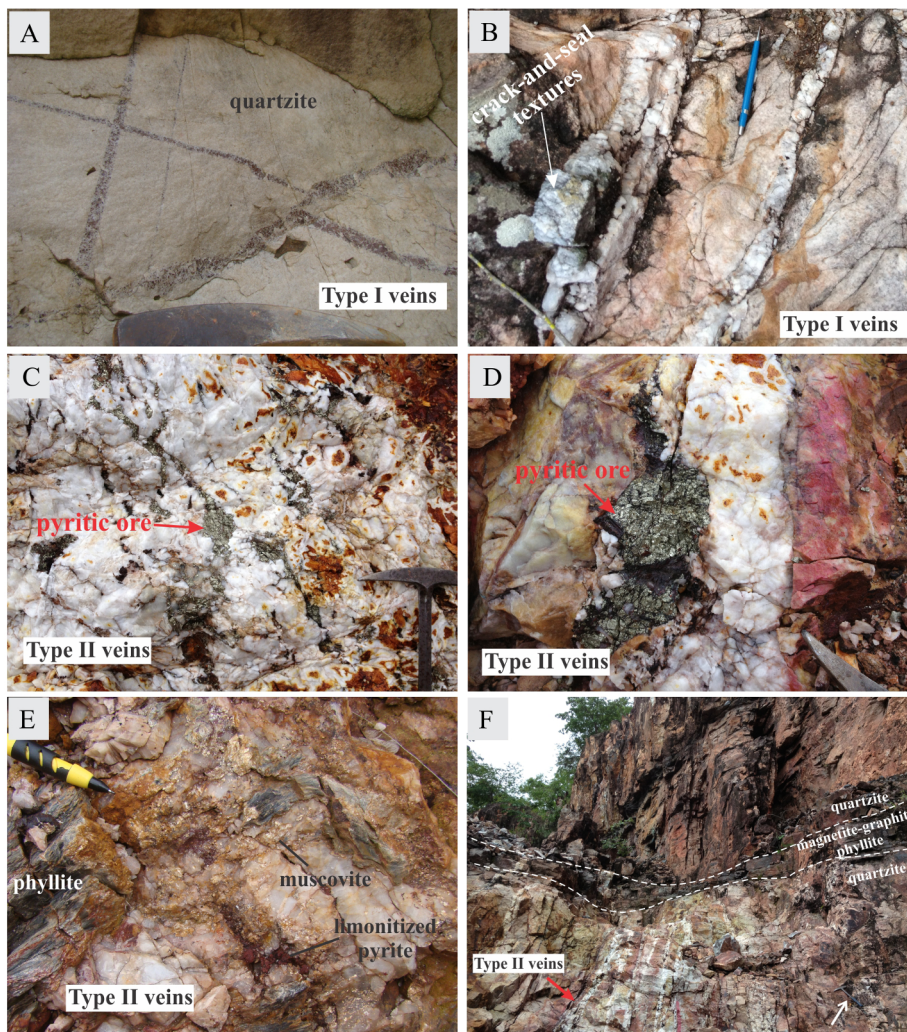### 3.4. Major and trace elements

After the SEM–EDS and XRD characterization, major elements of inclusion-free pyrite separates were determined by X–Ray Fluorescence (XRF) at CETEM/RJ, using a Panalytical AXIOS spectrometer in wave dispersion mode with Wave Dispersive Spectrum detector. The sulfur content was determined by Dumas combustion (LECO SC632) and Loss On Ignition (LOI) by thermal gravimetry analysis (LECO TGA 701). Trace elements (in pyrite and pyrrhotite) and REE (in pyrite, pyrrhotite and muscovite) contents were determined by Inductively Coupled Plasma Mass Spectrometry (ICP-MS; using a Perkin Elmer ELAN DRCII ICP) at Université de Nice, France. For this purpose, we used powders of sulfides and muscovite (50 mg) that were acid digested in ultrapure HNO_3 and HF or HCl (e.g., Renac et al., 2010). The evaporated solution (70 °C) and the remaining precipitates were dissolved in HNO_3 (1%) for analysis. Concentrations (ppm) were then normalized to the NASC standard (cf. Gromet et al., 1984).

3.5. Raman spectroscopy

Raman spectroscopy was conducted in the carbonaceous material in phyllites (graphite) and for the identification of fluid phases in fluid inclusions (see below). For this purpose, we use a Horiba Jobin–Yvon LabRam HR Raman spectroscope with a He-Ne laser (632.8 nm at room temperature) at CETEM/RJ. For graphite thermometry, we use the equation of Beyssac et al. (2002) improved by Lünsdorf et al. (2013) on Raman spectrograms of graphite crystals. The Raman curve–fitting was conducted using lorentzian peak shapes as suggested for low–grade metamorphic samples by the aforementioned authors.

Table 1
Summary of structural features and tectonic setting of the Buracão area (after Pires et al., 2016).

Deformational phase	D1 phase		D2 phase	
Paleostress reconstruction	sub-horizontal E-W compression		subvertical ENE-WSW dextral transpressive system	
Stages	D_{1a} stage	D_{1b} stage	D_{2a} stage main stage	D_{2b} stage reactivation at shallow crustal level
Interpretation	progressive deformation from D_{1a} to D_{1b} stages			
Rheology	ductile	ductile-brittle	ductile-brittle	brittle
Structures	The main low-angle (< 40°), E or W dipping, S_{1a} continuous cleavage, coincident with the axial plane of centimeter-size F_{1a} isoclinal intrafolial folds in S_0 bedding ($S_{1a}//S_0$);	The main N-S trending open asymmetrical east-verging F_{1b} folds with the development of S_{1b} axial plane foliation dipping at low- to high-angles to the E or W (disjunctive spaced fan cleavage), and low-angle b_{1b} axes. The F_{1b} folds deform $S_{1a}//S_0$ and are widely recognized in the Buracão area.	NNE-trending High Deformation Zones (HDZ; with up to 150 m width) cross-cutting all the D_1 structures. In these zones, F_{1b} folds become tight to isoclinal, and $S_{1a}//S_0$ foliations become vertical. Development of meter-size NW-trending open F_{2a} folds with S_{2a} axial planes dipping at low- to intermediate angle to the NE or SW, and b_{2a} axes plunging at low-angle to the SE. These folds are scarce and are associated with steep limbs of F_{1b} folds at the HDZ;	N40°E and N20°E oblique (dextral-normal/reverse) and less abundant W-E and N45°W sinistral shear fractures. They show surfaces containing steps and slickenlines or zones of tectonic breccias. Development of associated extensional fractures at N60°E, N80°E and N-S trends;
Relation with the regional tectonics of the Brasília Fold Belt (BFB)	Low-angle continuous cleavage related to the development of crustal-scale N-S trending, east-verging thrust fronts in the early collisional stage recorded regionally in the northern BFB;	The main regional N-S trending, east-verging folding regionally recorded in the northern BFB. This is resulted in the progression of shortening produced by the D_{1a} thrust fronts;	The HDZ and associated structures are local structures that reflect regional-scale N-S and NE-trending, oblique-dextral, subvertical transpressive shear zones in the external domain of BFB;	D_{2b} structures occur locally. Lack of regional equivalents;
Metamorphism	Metamorphic peak at greenschist facies (biotite zone; 425 to 500 °C);	Syn- to late metamorphic peak;	Post metamorphic peak;	Post metamorphic peak;
Vein system	Type I barren veins;		Type II ore veins;	
Geometry and Kinematics	Veins represent subvertical conjugated shear (Fig. 2A) and narrow extensional (Fig. 2B) fractures: N70°E (dextral), N50°W (sinistral) and N-S (extensional) trends;		Veins represent sets of subvertical shear fractures: N50°E, N20°E and N-S (dextral) and W-E (sinistral) trends;	
Related structures	Shear fractures occur along F_{1b} fold limbs, while extensional fractures along hinge zones of F_{1b} folds with associated stockwork zones;		Shear fractures occur spatially and geometrically associated to subvertical NNE-trending HDZ and related F_{2a} folds;	
Interpreted structural model	Fracture system generated during folding of competent quartzite beds;		Riedel shear fracture system related to a main dextral transpressive system;	
Thickness	up to 60 cm thick;		up to 3 m thick;	
Ore mineralogy	absent;		Pyrite + hematite ± magnetite ± pyrrhotite + gold;	
Gangue mineralogy	Quartz, muscovite;		Quartz, muscovite ± carbonate; Massive;	
Textures and internal structures	Zoned: Crack-and-seal textures (Fig. 2B); Sucessive microcrystalline, saccharoidal and anhedral bulk milky quartz in their outer zones, and druzy quartz (comb) in their inner zones;		Homogeneous textures, with massive or disseminated sulfide ore randomly grown with anhedral bulk milky quartz and muscovite (Fig. 2C, D and E). Minor portions of saccharoidal textures;	

Fig. 2. Textures and field relations of type I and II veins. *Type I barren veins* represent (A) a set of conjugated shear fractures and (B) extensional fractures with crack–and–seal textures and unidirectional quartz growth (hammer 15 cm length; pencil: 15 cm length). *Type II ore–bearing veins* are composed of (C) randomly intergrowth of anhedral bulk milk quartz and massive pyritic ore (D: detail; hammer: 25 cm length); (E) detail of textural growth of quartz, muscovite and pyrite (limonitized) in type II (pencil: 10 cm length); (F) intercalation of graphite–magnetite phyllite within the Quartzite Unit, which hosts type II ore–bearing veins (hammer: 40 cm length, white arrow).

3.6. Fluid inclusions

We conducted fluid inclusion studies on seven double–polished thick sections of quartz from barren and ore–bearing veins. Petrography was used to recognize the Fluid Inclusion (FI) Assemblages (primary or secondary; e.g., Goldstein and Reynolds, 1994); followed by Raman spectroscopy (at room temperature) for the identification of carbonic and solid phases. We measured the proportion of fluid phases in each FIA by image analyses of photomicrographs. Then, microthermometric runs were conducted at CETEM/RJ using a calibrated Linkam TP–92 freezing–heating stage on different fragments for each FIA analyzed. The measured temperatures were then used for calculations/data treatments using the package *FLUIDS* 1 (i.e., *BULK*, *Q2* and *ISOC*; Bakker, 2003) and HOKIEFLINCS_H2O-NACL softwares (Steele-MacInnis et al., 2012). The whole dataset was treated statistically through boxplot systematics with the representation of the interquartile range and the minimum/maximum values represented by the whiskers.

We measured the eutectic (Te), solid melt (i.e., Tm_{CO_2}, Tm_{ice}, $Tm_{clathrate}$ and Tm_{halite}) and the homogenization temperatures (i.e., Th_{CO_2} for carbonic phase and Th_{tot} for bulk fluid inclusion) during microthermometric measurements. They were used to estimate the pressure of homogenization (Ph_{CO_2} and Ph_{tot}) as well as fluid salinity (cf. Bodnar, 1993 for aqueous FI; cf. Haar et al., 1984 for medium salinity aqueous–carbonic FI and cf. Bodnar, 2003 for halite–bearing FI) and total homogenization density (Dh_{tot}; cf. Zhang and Frantz, 1987 for aqueous FI and cf. Duan et al., 1992a,b for aqueous–carbonic FI). Density of carbonic phase (Dh_{CO_2}) was determined cf. Thiery et al.

(1994). The CH_4 proportion in carbonic phase was calculated using Tm_{CO_2} and Th_{CO_2} from each fluid inclusion (cf. Heyen et al., 1982).

4. Results

### 4.1. Petrography and mineralogy of host rocks

4.1.1. Host rocks

Quartzites from the Quartzite Unit (QU) are massive and show mostly a white saccharoidal texture (Fig. 3A), locally preserving their original characteristics such as well sorted, fine–grained, rounded quartz grains. Phyllites from the Upper (UPU) and Lower (LPU) phyllite units (Fig. 3B) and those from the intercalation of the QU are dominantly composed of quartz, $2 M_1$-*tv* muscovite (FWHM = 0.11–0.16 °2Θ; Appendix 1), ferroan chlorite, biotite, euhedral Ti-rich magnetite and pockets of graphite particles (Fig. 3C, D and E; Appendix 1 and 2). The accessory minerals are hematite, rutile, tourmaline, monazite, xenotime and sulfides such as pyrite, chalcopyrite and sphalerite (Fig. 3F–H). In these phyllites, the variable proportions of quartz and mica define a sedimentary lamination (S_0; < 1 cm), which is parallel to the main S_{1a} slate cleavage ($S_{1a}//S_0$; Fig. 3B).

Petrographic observations show that magnetite is syn– to post–S_{1a} and pre–S_{1b}, i.e., it includes trails of quartz inclusions along S_{1a} and deflects S_{1b} crenulation (Fig. 3E and F). Similarly to biotite porphyroblasts, pockets of graphite (Fig. 3D) and some of the euhedral rutile, tourmaline, monazite and xenotime crystals also occur along the S_{1a}

Host rocks

Hydrothermally altered host rocks

Vein textures
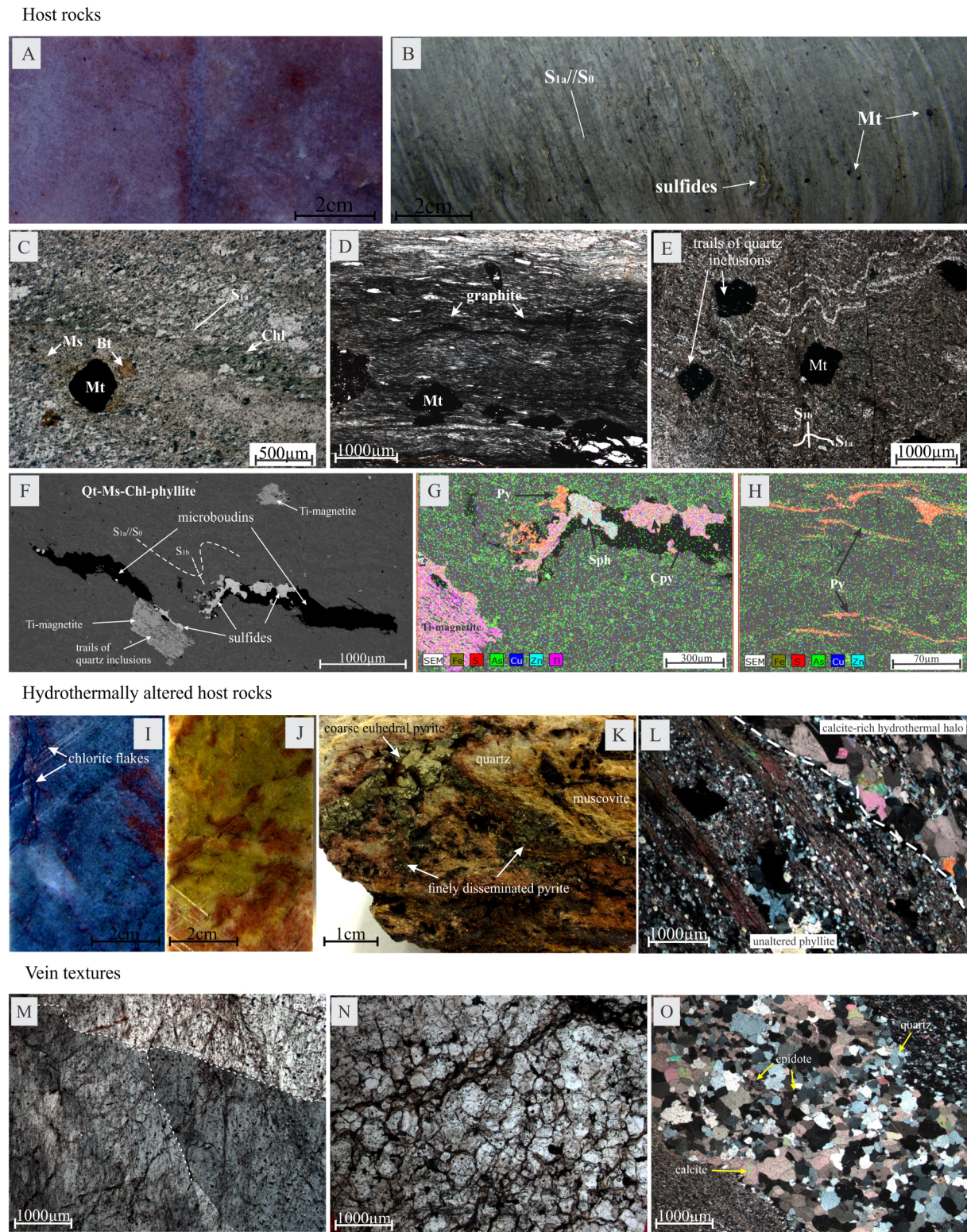
Fig. 3. Macroscopic and microscopic (optical and SEM–EDS) aspects of host quartzites–phyllites, hydrothermally altered rocks and type II quartz veins. *Host rocks*: macroscopic aspects of (A) white, well sorted, fine–grained quartzite (QU) and (B) greenish quartz–muscovite–chlorite phyllite (LPU) with magnetite crystals (Mt) and sulfides along the main $S_{1a}//S_0$; (C), (D) and (E) photomicrographs (PL) of (C) quartz–muscovite–chlorite phyllite showing biotite porphyroblasts (Bt), muscovite (Ms) and chlorite (Chl) also along S_{1a}, as well as (D) detail of graphite pockets and magnetite along this foliation; (E) euhedral magnetite that includes trails of quartz inclusions along S_{1a} and deflect the S_{1b} crenulation cleavage (photomicrograph; PL); (F) backscattered electrons SEM image showing structural relations of sulfide microboudins along $S_{1a}//S_0$ foliation and deformed by S_{1b} crenulation; (G and H) SEM–EDS multi–element chemical maps showing intergrowth of pyrite (Py) and lesser chalcopyrite (Cpy) and sphalerite (Sph) filling microboudins, as well high–Ti content in magnetite. *Hydrothermally altered host rocks*: macroscopic aspects of (I) chlorite–bearing greenish, (J) muscovite–bearing yellowish and (K) pyrite–muscovite–bearing hydrothermal alteration developed in host quartzite; (L) boundary (dotted line) between calcite–free unaltered phyllite and calcite–rich hydrothermal alteration halo (photomicrograph; PL). *Type II quartz veins* show homogeneous textures such as (M) coarse–grained anhedral bulk milky quartz, (N) fine–grained saccharoidal quartz and (O) photomicrograph of saccharoidal quartz with calcite and epidote crystals (polarized light = PL).
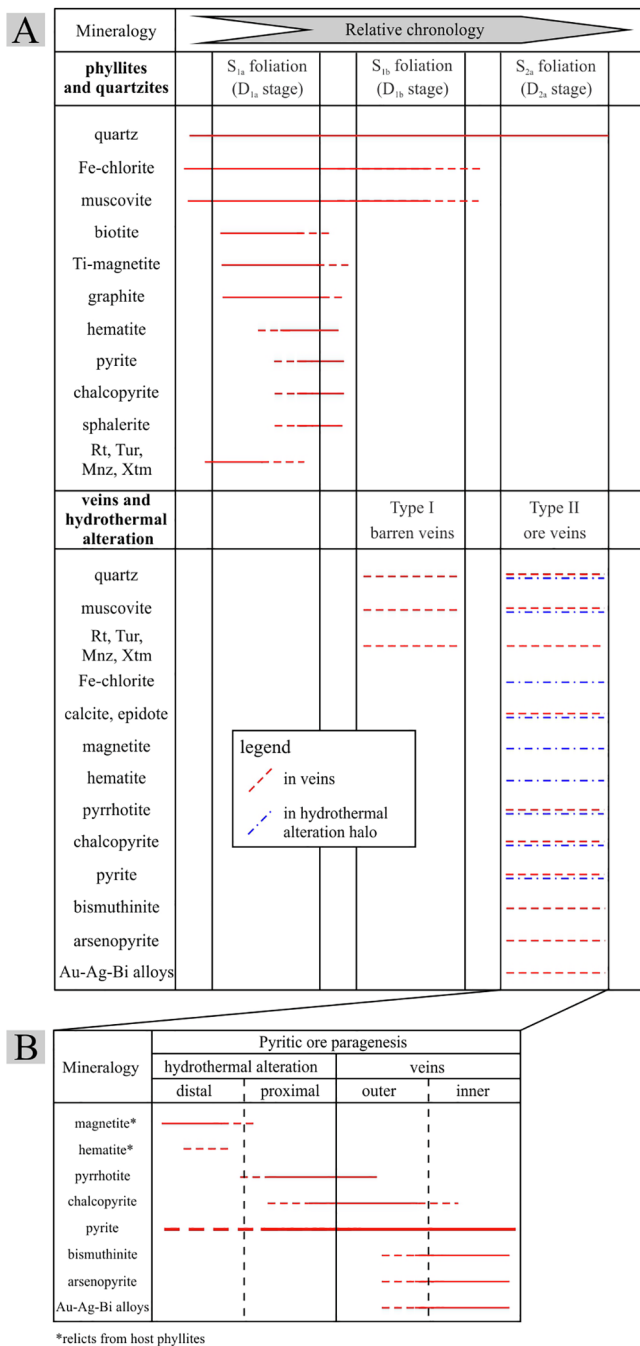
Fig. 4. (A) Chronological relations between mineral phases and tectonic foliations (deformational stages) in host quartzites and phyllites as well as in type I and II veins and related hydrothermal alteration halos; (B) paragenetic sequence of mineral phases distributed in the pyritic ore along type II veins and related hydrothermal alteration halos (Rt: rutile; Tur: tourmaline; Mnz: monazite; Xtm: xenotime).

slaty cleavage (Fig. 4A). The SEM–EDS observations also revealed microboudins concordant with $S_{1a}//S_0$ slaty cleavage and deformed by S_{1b} crenulation (Fig. 3F); quartz is intergrown with anhedral sulfides such as pyrite with trace of Bi, as well as lesser amounts of chalcopyrite and sphalerite (Fig. 3G and H; Appendix 3), while magnetite crystals near these structures are replaced by hematite rims.

4.1.2. Hydrothermally altered host rocks

The hydrothermal alteration is better expressed in the outer border of type II ore–bearing veins (Fig. 4A), where host rocks show greenish

to yellowish alteration halos with a width up to 1 m. In quartzite, the hydrothermal alteration assemblage with a greenish color shows granoblastic quartz with ferroan chlorite flakes (Fig. 3I and Appendix 1). The yellowish halo has coarser–grained $2 M_1$-tv muscovite than white unaltered quartzite (Fig. 3J) and coarse–grained euhedral to finely disseminated pyrite crystals (Fig. 3K). In phyllites, hydrothermal halos contain calcite (Fig. 3L) and centimeter–size euhedral pyrite associated with a mixture of coarse ferroan chlorite and $2 M_1$-tv muscovite flakes overgrowing those formed along the S_{1a} and S_{1b} cleavages (Fig. 4A and Appendix 1). Thus, the alteration halos are mostly distinguished from unaltered host rocks by (i) mineral grain-size, which is coarser in alteration halos; (ii) crystal habit, e.g., pyrite in alteration halo is euhedral and occurs in larger proportions; and (iii) the occurrence of calcite.

4.2. Texture and mineralogy of barren type I and ore–bearing type II quartz veins

The barren quartz veins (termed "BV" here) show heterogeneous textures composed of microcrystalline, saccharoidal or anhedral bulk milky quartz with coarse–grained and well crystallized $2 M_1$-tv muscovite (FWHM = 0.11–0.16 °2 Θ; Appendix 1). Their accessory minerals are millimeter–size euhedral rutile, hematite, tourmaline, monazite and xenotime, similarly as described in quartzite–phyllite host rocks. The ore–bearing quartz veins (termed "OV" here) show homogeneous textures such as (i) coarse–grained, anhedral bulk milky quartz with quartz crystals larger than 1 cm (Fig. 3M); or (ii) less abundant fine–grained saccharoidal quartz with quartz crystals shorter than 1 mm (Fig. 3N). Both quartz textures (i) and (ii) show dominant quartz with coarse--grained, well crystallized $2 M_1$-tv muscovite (FWHM = 0.11–0.16 °2 Θ; Appendix 1) ± fine–grained calcite. Finer-grained, euhedral epidote locally occurs with calcite (Fig. 3O), where veins cross–cut phyllite layers, and with associated calcite–rich hydrothermal halos (Fig. 3L). Their accessory minerals are the same described in type I barren veins. Quartz–muscovite ± calcite and accessory minerals represent 60–80% (in vol.) of the ore–bearing veins, and occur as an intergrowth with euhedral to massive anhedral pyritic ore (40 –20%).

The ICP–MS analyses of white mica separates from barren and ore–bearing veins indicate that muscovite from both vein types have a similar low REE concentration (ΣREE 0.58–0.76 ppm; Appendix 3). The REE patterns are flat (La_N/Yb_N ~ 0.001) with slight enrichment in Ce and Lu and positive Eu anomaly (Eu/Eu*: 10–16.67) when normalized to the NASC (Fig. 5 and Appendix 3). Although no mineral inclusion have been identified by XRD in these white mica separates, the enrichment in Ce and Lu may suggest the local presence of REE–rich microinclusions.
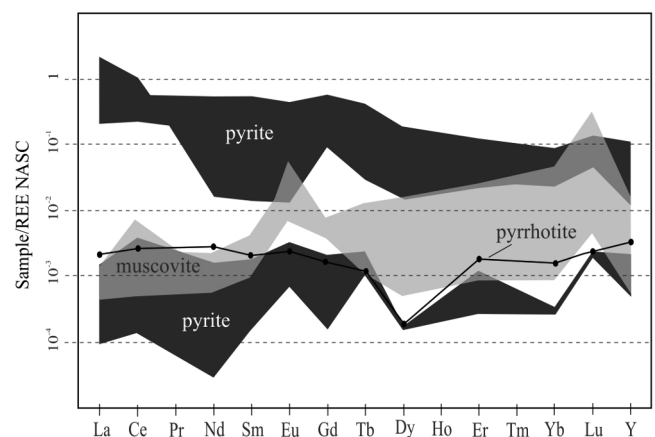
Fig. 5. NASC–normalized REE pattern of muscovite, pyrite and pyrrhotite from ore–bearing veins (NASC after Gromet et al., 1984).
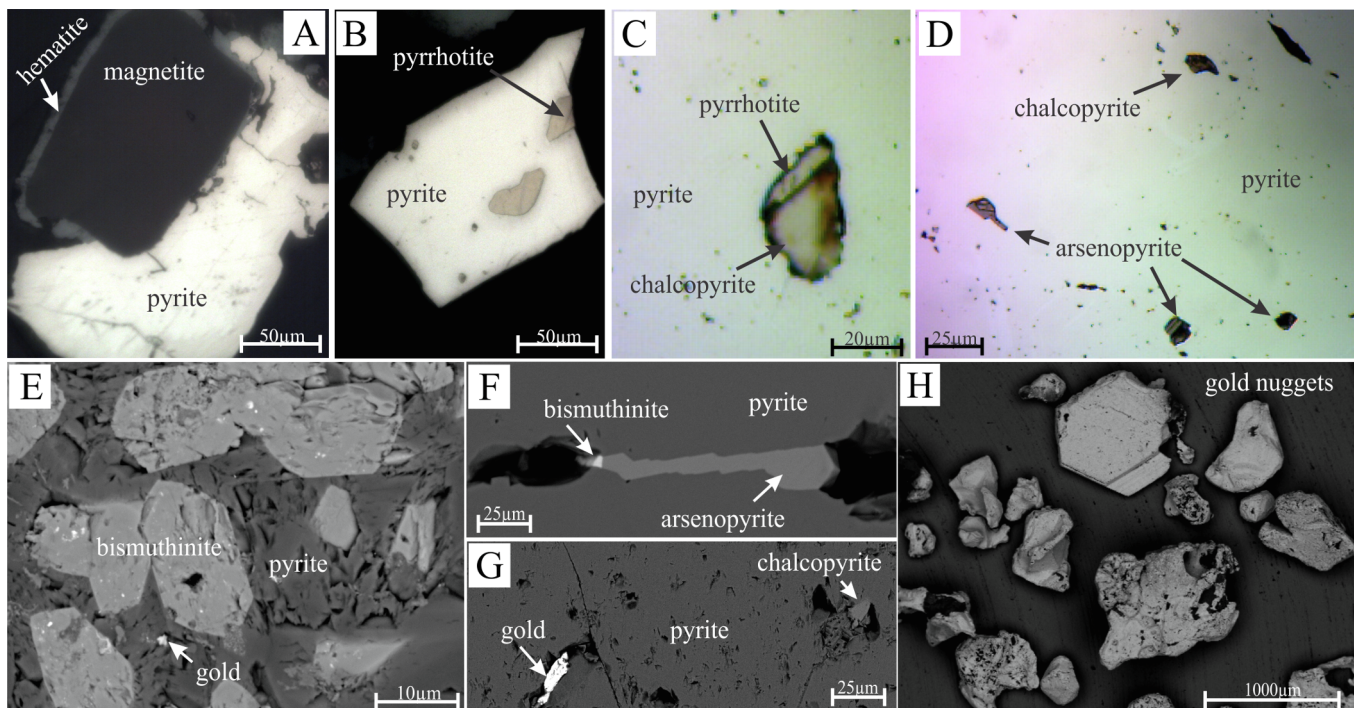
Fig. 6. Mineralogy, textures and gold grain morphologies in the pyritic ore. Reflected light photomicrographs show mineral textures of pyritic ore such as (A) euhedral magnetite with hematite rims, both included within pyrite; (B) pyrrhotite inclusions within pyrite; (C) pyrite with inclusions of pyrrhotite + chalcopyrite; and (D) pyrite with inclusions of arsenopyrite. Backscattered electrons SEM image show association of (E) euhedral bismuthinite with free gold; (F) arsenopyrite and bismuthinite; and (G) chalcopyrite and free gold, all included within pyrite; (H) gold grains show irregular morphologies and hexagonal shape.

4.2.1. Mineralogy, textures and chemical composition of the pyritic ore

Petrography of pyritic ore shows an assemblage dominated by massive pyrite (Fig. 6; Py) with micrometer- to centimeter-size inclusions of arsenopyrite (Asp), pyrrhotite (Po), chalcopyrite (Cpy), bismuthinite (Bsm), magnetite (Mt), hematite (Hm) and free gold nuggets, in decreasing amounts. These inclusions are dominantly anhedral with irregular to rounded shapes, although rare euhedral inclusions have been found.

Different pyrite inclusion associations are recognized in the transition from distal to proximal alteration halos in host rocks (with up to 1 m width) and into pyritic ore in veins (with up to 3 m width; Fig. 4B). It is important to note that these mineral changes are so gradual that it is virtually impossible to observe all of them in the same polished section, so the descriptions below are based on several panned mineral concentrates and polished thin sections from the same or different locations. In the distal hydrothermal halos (Fig. 4B), euhedral magnetite with hematite rims is present (Fig. 6A), which probably remained from the host phyllites. Magnetite is surrounded by massive pyrite of the pyritic ore, which becomes richer in pyrrhotite inclusions (Fig. 6B) as magnetite and hematite become less abundant. In the proximal halos and in type II quartz veins (Fig. 4B), pyrite shows mostly inclusions of anhedral/rounded pyrrhotite and chalcopyrite (Fig. 6C). Based on different samples, in the transition from distal to proximal hydrothermal alteration halos (Fig. 4B), Mt and Hm inclusions become progressively scarce and eventually disappear, while Po and Cpy become abundant. Pyrrhotite and Cpy inclusions are more abundant in pyrite from the outer zones of ore veins, while inclusions of arsenopyrite (Fig. 6D), bismuthinite and free gold nuggets are prominent in their inner zones (Fig. 4B). There is also an association between inclusions of Asp, Bsm and gold within pyrite (Fig. 6E and F), locally associated with Cpy inclusions (Fig. 6G). The SEM–EDS shows that pyrite in contact with Asp and Bsm also has traces of As and Bi in solid solution, and Asp [$Fe_{(1.0)}As_{(0.8–0.9)}S_{(1.1–1.3)}$] has between 28.8 and 30.4 at.% of arsenic (expressed in the interquartile range; Appendix 3). In addition to the presence of free gold and inclusions in sulfides, pyrite and associated

arsenopyrite also contain up to 0.5 wt% and 1.2 wt% of structural gold, respectively (Appendix 3).

The chemical composition of pyrite (Appendix 3) shows typical proportions of Fe (49.8–56.7 wt%) and S (42.2–49.4 wt%) with traces of Bi and As [$Fe_{(0.9–1.0)}As_{(0–0.02)}Bi_{(0–0.02)}S_{(1.9–2.3)}$]. Pyrite in association with (α) pyrrhotite and magnetite shows low trace element contents of Bi, As, Se (S/Se: 16,678; Appendix 3), while pyrite associated with (β) arsenopyrite and bismuthinite is richer in As, Ag, Pb, Bi, Cu, Te and Se (S/Se: 2273; Appendix 3). Pyrite from both associations has low Pd and Pt contents.

Pyrite separates have variable REE contents (ΣREE: 0.01–140.5 ppm), and REE patterns normalized to the NASC (Fig. 5) show light REE enrichment (La/Yb$_N$: 7–70) and a slight negative Eu anomaly (Eu/Eu*: 0.32–0.79; Appendix 3). In comparison, pyrrhotite crystals have low REE contents (ΣREE: 0.38 ppm) and a flat REE pattern with strong Dy depletion (Fig. 5). The variability of the ΣREE contents is essentially related to high values in three samples (MIN-24B, -206A and -01A; Appendix 3). Although no mineral inclusions have been identified by SEM–EDS petrography and XRD in the sulfide separates, these high contents may suggest an influence of REE–rich microinclusions. In any case, both samples with low or high REE contents show similar flat NASC–like patterns (Fig. 5).

Both coarse free gold nuggets (up to 0.5 cm size) and structural gold in pyrite–arsenopyrite are recognized in pyritic ore by SEM–EDS petrography. With this technique, it is possible to distinguish microinclusions of free gold and structural gold "invisible" in micrometer scale. Binocular observations coupled with SEM–EDS petrography of gold grains revealed different irregular morphologies, besides rare euhedral hexagonal grains (Fig. 6H). These different gold grains are Au–Ag–Bi alloys, classified as native gold with 80% of them with Fn higher than 800, and subordinately by electrum – Fn from 600 to 800.

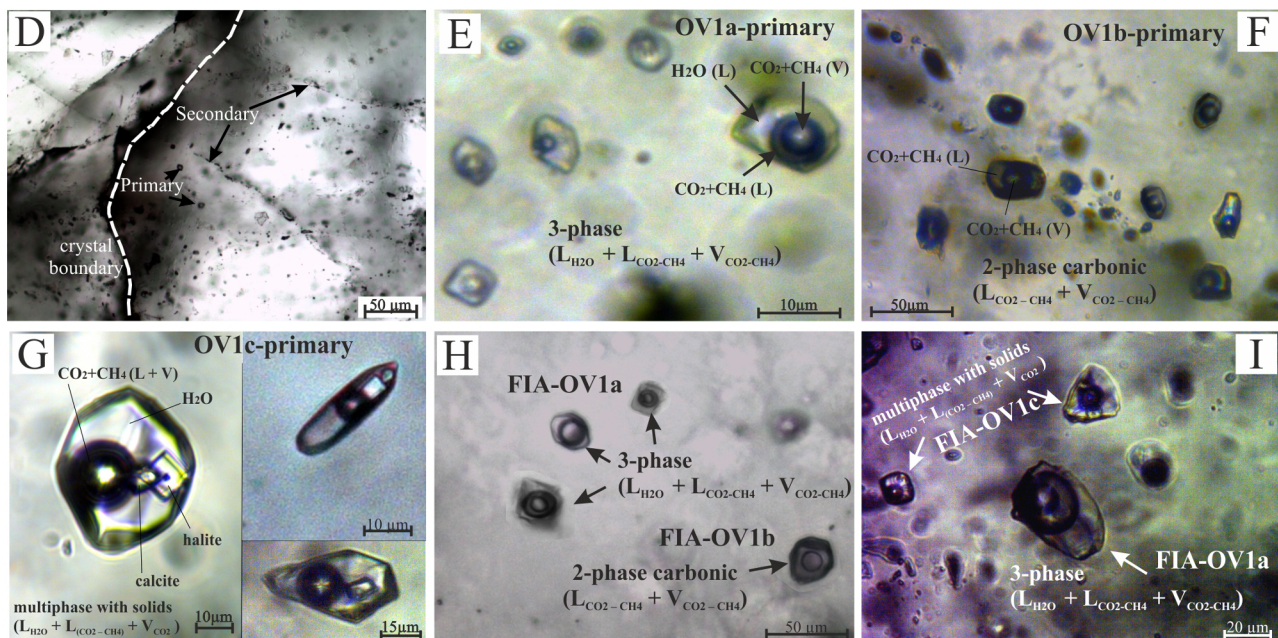### 4.3. Fluid inclusions in syn-D$_{1b}$ type I barren quartz veins

The syn–D$_{1b}$ barren quartz veins show primary BV1 and later,
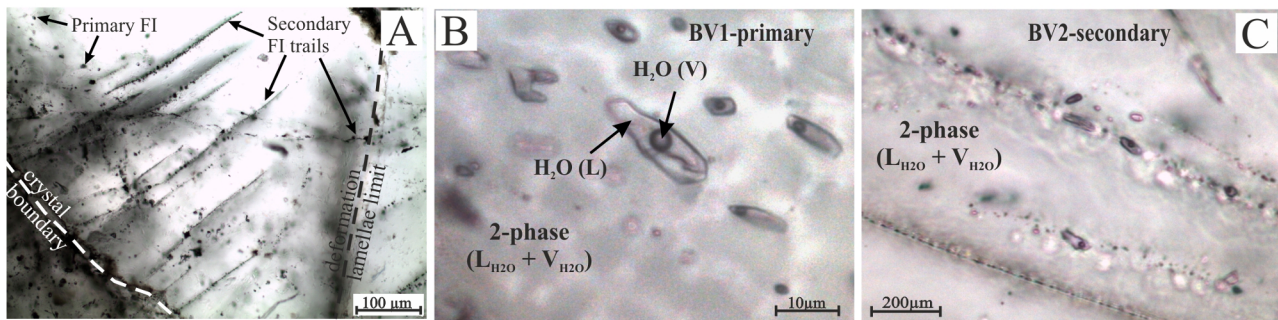
Fig. 7. Summary of fluid inclusion petrography in quartz from vein types. *Barren veins*: (A) petrographic relations between primary and secondary fluid inclusion assemblages (FIAs); detail of (B) primary (FIA-BV1) and (C) secondary (FIA-BV2) 2–phase aqueous fluid inclusions. *Ore–bearing veins*: (D) petrographic relations between primary (FIA-OV1) and secondary (FIA-OV2) fluid inclusion assemblages; detail of (E) primary 3–phase aqueous–carbonic (OV1a), (F) 2–phase carbonic (OV1b), and (G) multiphase aqueous–carbonic (OV1c) fluid inclusions; detail of the coexistence of FIAs OV1a and OV1b (H), and FIAs OV1a and OV1c (I) within the same quartz crystal.

secondary BV2 fluid inclusion assemblages (Fig. 7A). The FIA-BV1 shows rounded to negative–crystal shapes disposed randomly within quartz crystals (Fig. 7B). The FIA-BV2 are rounded and aligned in parallel trails along healed fractures associated with deformation lamellae within quartz crystals (Fig. 7C). Petrography and Raman analyses revealed that both BV1 and BV2 contain dominant 2–phase aqueous FI ($< 15\,\mu m$) with a constant degree of liquid infilling (F) of $\sim 90\%$.

The microthermometric data (Appendix 4), after statistical treatment (i.e., the interquartile range), are shown in Table 2 and Fig. 8. These FIAs show similar ranges of Te (-21.8 to $-21.6\,°C$) and Tm_{ice} (-8.2 to -7.6 and -8.5 to $-7.0\,°C$ in BV1 and BV2, respectively). The total homogenization temperature to the liquid phase (i.e. $Th_{tot\,L+V\rightarrow L}$) is higher for primary (BV1: $350–368\,°C$) than for secondary (BV2: $196–227\,°C$) populations. The Te and Tm_{ice} indicate H_2O–NaCl–dominated compositions, and both FIAs show the same salinity range (e.g., $11.2–11.9$ and $10.5–12.3$ eq. wt% NaCl for BV1 and BV2, respectively). The bulk fluid density (i.e., fluid density estimated after Th_{tot}) is lower in primary than in secondary FI (i.e., $0.75–0.77$ and $0.94–0.95$ g/cc, respectively; see Table 2 and Fig. 8).

4.4. Fluid inclusions in syn-D_{2a} type II ore–bearing quartz veins

The syn–D_{2a} ore–bearing veins show primary FIA-OV1 with negative–crystal shapes, which are randomly arranged in anhedral quartz crystals (Fig. 7D). These primary fluid inclusions are shown with three different fluid proportions with decreasing abundance:

(a) OV1a: *3–phase aqueous–carbonic* (~ 50 to 56% H_2O_{liquid}; $\sim 37\%$ $Carbonic_{liquid}$; ~ 7 to 13% $Carbonic_{vapor}$ in vol.) FI with up to $35\,\mu m$ in size (Fig. 7E);

(b) OV1b: *2–phase carbonic* ($\sim 80\%$ $Carbonic_{liquid}$; $\sim 20\%$ $Carbonic_{vapor}$ in vol.) FI with up to $25\,\mu m$ size (Fig. 7F), with a low proportion of aqueous phase ($H_2O_{liquid} < 5\%$);

(c) OV1c: *Multiphase aqueous–carbonic* ($65–74\%$ H_2O_{liquid}; $13–20\%$ $Carbonic_{liquid}$; $4–6\%$ $Carbonic_{vapor}$ in vol.) FI, smaller than $30\,\mu m$ size, with one or rarely two daughter minerals: an isotropic cubic crystal ($\sim 7\%$ in vol.) and other rare rhombohedral crystals with high birefringence and relief ($\sim 2\%$ in vol.; Fig. 7G).

The FI types observed with variable proportions of their components

Table 2
Summary of the fluid inclusion microthermometry.

Barren veins

FIA-BV1(P) and FIA-BV2(S): 2-phase aqueous FI (H_2O_{liquid} + H_2O_{vapor})

	Measured			Calculated			
	Te (°C)	Tm$_{ice}$ (°C)	Th: L + V → L (°C)	Salinity (eq. wt.% NaCl)	Dh$_{tot}$ (g/cc)	Ph$_{tot}$ (kbar)	dP/dT (bar/°C)
P (n = 21)	−21.8 to −21.6	−8.2 to −7.6	350.0 to 368.0	11.2 to 11.9	0.75 to 0.77	0.11 to 0.14	7.9 to 12.6
S (n = 26)	−22.1 to −21.7	−8.5 to −7.0	196.0 to 227.0	10.5 to 12.3	0.94 to 0.95	0.01 to 0.02	13.1 to 18.2

Ore-bearing veins

FIA-OV1a: 3-phase aqueous-carbonic FI (H_2O_{liquid} + $Carbonic_{liquid}$ + $Carbonic_{vapor}$)

	Measured						Calculated						
	Tm$_{CO2}$ (°C)	Te (°C)	Th$_{CO2}$: L + V → L (°C)	Tm$_{clathrate}$ (°C)	Th$_{CO2}$: L + V → L (°C)	Th$_{tot}$: L + V → L (°C)	mol % of CH$_4$ in carbonic phase	Dh$_{CO2}$ (g/cc)	Ph$_{CO2}$ (kbar)	Salinity (eq. wt.% NaCl)	Dh$_{tot}$ (g/cc)	Ph$_{tot}$ (kbar)	dP/dT (bar/°C)
P (n = 157)	−57.8 to −57.1	−22.1 to −21.2	22.9 to 27.9	6.8 to 7.5	26.2 to 28.6	260.0 to 345.0	6 to 12	0.59	0.09	9.3 to 10.6	0.84	1.2 to 2.5	14.7 to 15.0

FIA-OV1b: 2-phase carbonic FI ($Carbonic_{liquid}$ + $Carbonic_{vapor}$)

	Measured		Calculated		
	Tm$_{CO2}$ (°C)	Th$_{CO2}$: L + V → L (°C)	mol % of CH$_4$ in carbonic phase	Dh$_{CO2}$ (g/cc)	Ph$_{CO2}$ (kbar)
P (n = 120)	−58.2 to −57.1	22.9 to 27.9	6 to 12	0.59	0.09

FIA-OV1c: multiphase aqueous-carbonic FI (H_2O_{liquid} + $Carbonic_{liquid}$ + $Carbonic_{vapor}$ + $NaCl_{(s)}$ ± $calcite_{(s)}$)

	Measured						Calculated						
	Tm$_{CO2}$ (°C)	Te (°C)	Th$_{CO2}$: L + V → L (°C)	Tm$_{halite}$ (°C)	Th$_{CO2}$: L + V → L (°C)	Th$_{tot}$: L + V → L (°C)	mol % of CH$_4$ in carbonic phase	Dh$_{CO2}$ (g/cc)	Ph$_{CO2}$ (kbar)	Salinity (eq. wt.% NaCl)	Dh$_{tot}$ (g/cc)	Ph$_{tot}$ (kbar)	dP/dT (bar/°C)
P (n = 29)	−58.0 to −57.1	−22.0 to −21.3	22.6 to 28.5	112.5 to 142.0	295.0 to 344.0		7 to 11	0.59	0.09	28.3 to 29.3	0.95 to 1.00	2.0 to 2.8	14.5 to 14.7

P = primary, S = secondary, n = number of measurments
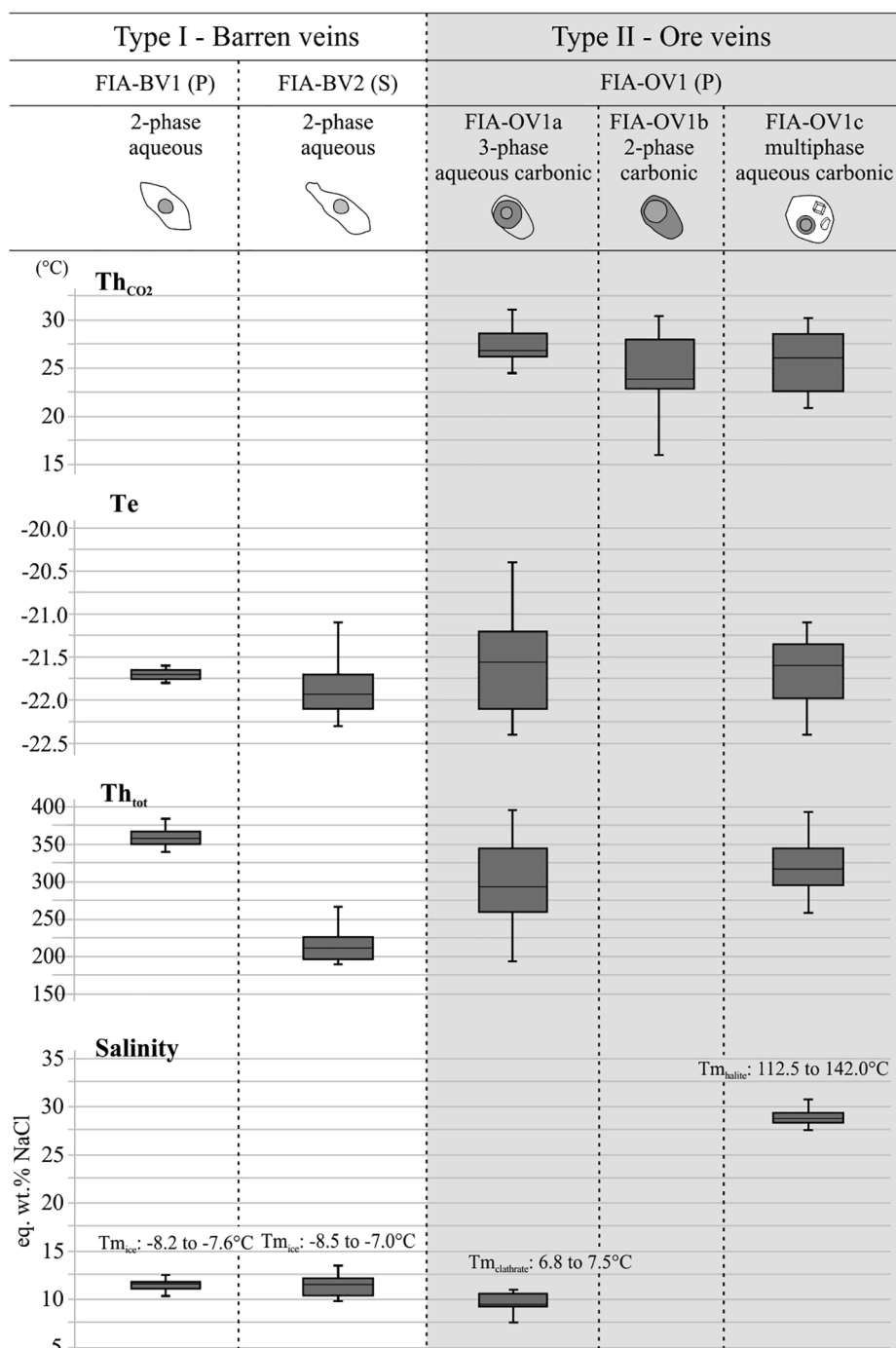
Fig. 8. Boxplot presentation of fluid inclusion microthermometric data from barren and ore–bearing veins: homogenization temperature of carbonic phase (Th_{CO2}), eutectic temperature (Te), total homogenization temperature (Th_{tot}) and calculated salinity based on the solid melt temperatures: Tm_{ice}, Tm_{halite} and $Tm_{clathrate}$. P: primary; S: secondary.

or degree of fill (F) show no evidence of necking–down or leakage, which rules out post-entrapment FI modifications. The three OV1 types occur randomly disposed within the same quartz crystal (e.g., Fig. 7H and I), without fractures, deformation and recrystallization of host quartz; with the exception of scarce FIA-OV2 that comprise aqueous and carbonic one–phase FI (< 10 μm), observed only in few samples.

Raman spectroscopy shows that the liquid carbonic phase (Carbonic$_{liquid}$) from all OV1 types consists of mixtures of CO_2 (± $^{13}CO_2$) with minor CH_4, without CO, O_2, H_2, N_2 or SO_2 (Appendix 2). The CO_2 Fermi diad split (Δ, cm^{-1}; cf. Wang et al., 2011) varies from 103.4 to 104.6 cm^{-1}. The shift of diad indicates varying densities

of these carbonic mixtures between 0.28 (103.4 cm^{-1}) and 0.83 g/cc (104.6 cm^{-1}; Appendix 2), the last associated with the higher intensity of the CH_4 peak. Moreover, rhombohedral shape daughter minerals (FIA-OV1c) are identified as calcite (Appendix 2), whereas cubic crystals did not produce a good response to Raman excitation. Further, these last crystals have been identified as salts by their melting point. The FIA-OV2 secondary one–phase FI was not analyzed during micro-thermometric measurements.

The FIA-OV1a and OV1c show similar range of total homogenization temperature (to the liquid state), i.e., $Th_{tot\ (L+V\ \pm\ S\rightarrow L)}$ of 260–345 and 295–344 °C, respectively (Table 2 and Fig. 8). All of these FI

populations also show Te in the same range (−22.1 to −21.2 °C), which indicates a similar NaCl–H_2O system for their aqueous phase. Their salinities were determined assuming a dominant NaCl–H_2O system with $Tm_{clathrate}$ (6.8–7.5 °C for OV1a) and Tm_{halite} (112.5–142.0 °C; $Tm_{halite} < Th_{tot}$ for OV1c), which allow calculation of salinities between 9.3–10.6 and 28.3–29.3 eq. wt% NaCl (Table 2 and Fig. 8).

The microthermometric data of the carbonic phase (liquid + vapor) of FIAs OV1a, OV1b and OV1c show a modal temperature of carbonic phase melt (Tm_{CO2}: −58.2 to −57.1 °C) and homogenization of carbonic immiscible phase to liquid ($Th_{CO2 (L+V→L)}$: 26.2–28.6, 22.9–27.9 and 22.6–28.5 °C, respectively) in the same range. The variation between these two temperatures is constant in all FI populations, and corresponds to ca. 6–12% mol of CH_4 in the carbonic phase with a bulk density of ∼0.59 g/cc (Table 2 and Appendix 4). The bulk fluid density calculated for FIA-OV1a and OV1c (i.e., after Th_{tot}) yielded a total fluid density of ∼0.84 and 0.95–1.00 g/cc, respectively.

5. Discussion

5.1. The syn-D_{1a-1b} metamorphic peak and type I barren veins
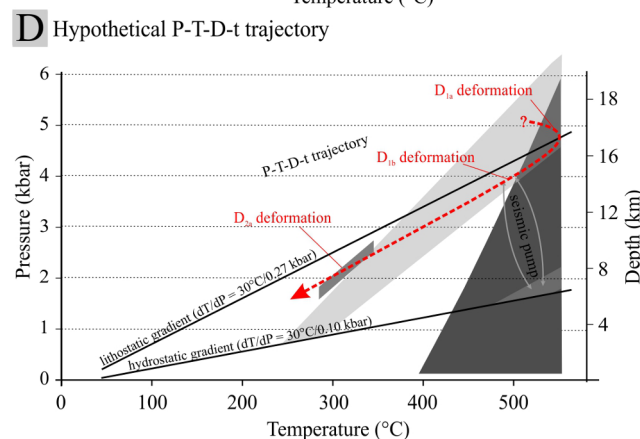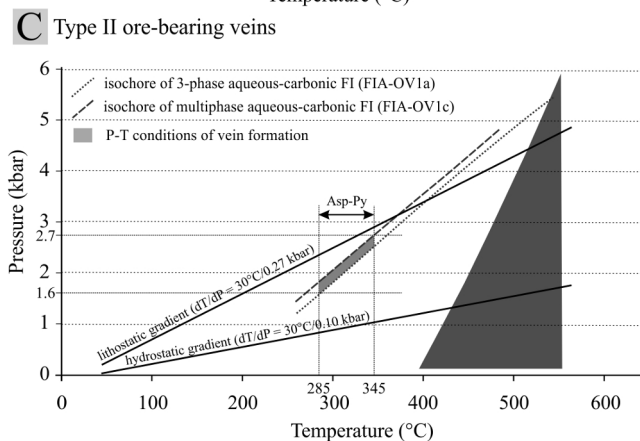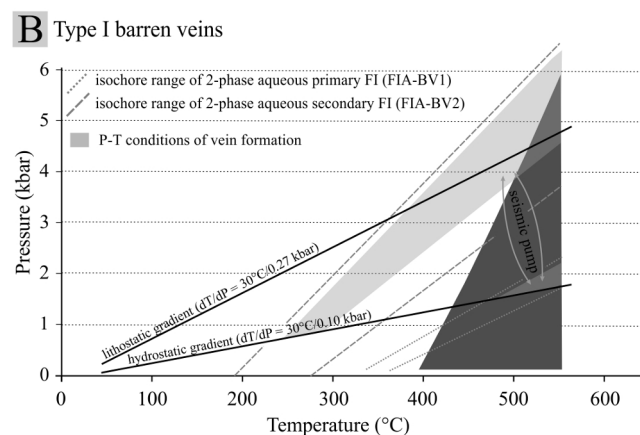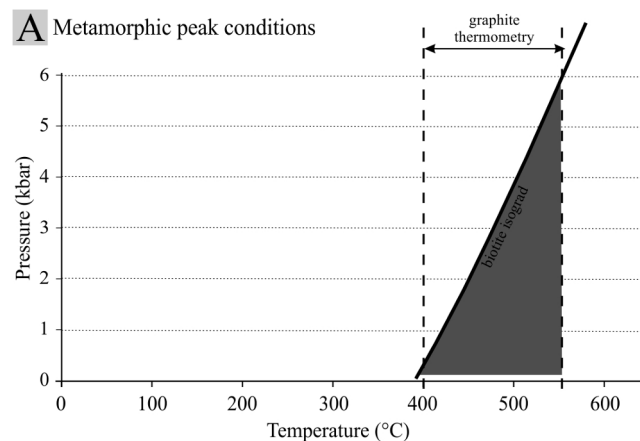
5.1.1. Metamorphism of the sedimentary pile

The similar metamorphic assemblage in phyllites from the lower (LPU) and quartzite (QU) units with biotite, ferroan chlorite, Ti–magnetite, sulfides and graphite suggests high-metal contents and the presence of organic matter in their protoliths.

The petrographic association between graphite and biotite along the S_{1a} slaty cleavage (syn–D_{1a} deformational stage; Fig. 4A) allows the application of the graphite thermometry (Beyssac et al., 2002; Lünsdorf et al., 2013) coupled with the biotite isograd to estimate the P–T conditions of the metamorphic peak in metapelites. The graphite thermometry yielded temperatures between 400 and 560 °C, which are consistent with those of the biotite metamorphic zone (425–500 °C; e.g., Best, 2003), and indicate a maximum pressure of 6 kbar for the graphite–biotite metamorphic peak at the Buracão area (Fig. 9A). Moreover, the predominance of syn–S_{1a} Ti–magnetite and graphite over Py and Hm in quartz–muscovite–chlorite phyllites (Fig. 4) suggest metamorphic peak under the magnetite–graphite buffer, i.e., fO_2 at 10^{-21} and 10^{-29}; estimated between QFM and graphite maximum stability curves (Fig. 10A).

Sulfides formed in dilatational sites (e.g., microboudins) might represent a local fS_2 increase, which may be associated with low amounts of H_2S–rich fluids concentrated along dilatational structures in phyllites during metamorphism. In this sense, pyrite would result directly from the interaction of H_2S–rich fluids with Fe–silicates or magnetite (e.g., Reed, 1997). The association of magnetite and pyrite may represent a reaction resulting from decreasing pressure and/or temperature at dilatational sites coupled with addition of H_2S–rich fluids, which favors pyrite precipitation. The local decrease of P–T conditions may have been also responsible for the transformation of magnetite into hematite close to these sites, which is consistent with hematite rims surrounding euhedral magnetite near sulfide–filled microboudins. These mineral transformations may be related to a combination of cooling and rock–buffering, where oxygen is buffered internally by the bulk–rock composition (e.g., Evans et al., 2006). Despite the insufficient data to fully constrain the origin of these fluids, it is reasonable to infer that they were derived from metamorphic devolatilization of the original pelitic pile since there is no clear evidence for an external fluid source; rather, the mineral assemblage and textures reflect an apparent equilibrium between fluids and percolated rocks.

5.1.2. Type I barren veins: fluid source(s), genetic processes and p_f–t_f–x pathways

The constant low-salinity H_2O–NaCl fluid inclusion composition and simple quartz–muscovite mineralogy suggest that silica–bearing aqueous fluids were responsible for the formation of type I barren veins. In comparison with primary FIA-BV1, secondary FIA-BV2 shows similar

A Metamorphic peak conditions

B Type I barren veins

isochore range of 2-phase aqueous primary FI (FIA-BV1)
isochore range of 2-phase aqueous secondary FI (FIA-BV2)
P-T conditions of vein formation

C Type II ore-bearing veins

isochore of 3-phase aqueous-carbonic FI (FIA-OV1a)
isochore of multiphase aqueous-carbonic FI (FIA-OV1c)
P-T conditions of vein formation

D Hypothetical P-T-D-t trajectory

(caption on next page)

Fig. 9. P–T–t evolution from metamorphic peak to type I and II vein formation. (A) Estimation of P–T conditions related to the metamorphic peak of the Buracão area: integration of graphite thermometry and biotite isograd in pelitic rocks. (B) P–T domains of barren type I vein during late–metamorphic peak: integration of litho- and hydrostatic gradients, and the main frequency of isochores of 2–phase aqueous primary and secondary FI. Note the discrepant P field for similar T range, suggesting a seismic pump system (see text for details). (C) P–T conditions of type II ore–bearing vein formation in post–metamorphic peak: integration of arsenopyrite–pyrite (Asp–Py) stability field, litho- and hydrostatic gradients and the main frequency of isochores of fluid inclusion assemblages-FIAs OV1a and OV1c aqueous–carbonic FI. (D) Idealized P–T–t trajectory for the study area. Depth inferred about lithostatic gradient (0.27 kbar/km).

←

H_2O–NaCl fluid compositions and salinity (10.5–12.3 and 11.2–11.9 eq. wt% NaCl, respectively; Table 2), but increasing density (0.94–0.95 and 0.75–0.77 g/cc, respectively; Table 2). The higher density of FIA-BV2 compared with BV1 is associated with higher dP/dT isochores (13.1–18.2 and 7.9–12.6 bar/°C, respectively; Table 2). The intercept of FIAs BV1 and BV2 isochores with hydrostatic and lithostatic gradients represent increasing pressure conditions from primary to secondary entrapments, but with similar range of minimal entrapment temperatures (which in part overlap those of the metamorphic peak; Fig. 9B). These P–T domains suggest that syn–D_{1b} type I barren veins were precipitated and deformed under syn- to late- metamorphic peak conditions (Fig. 9B). The structural relations between barren veins and F_{1b} folds (Table 1), coupled with varying SiO_2 solubility due to changing P-T conditions, suggest that the stress field related to folding could have generated over– and underpressurized sites, driving fluid influxes and inducing precipitation along extensional fractures with stockwork and crack–and–seal textures (Fig. 11A–C). Moreover, extensional fractures with lower internal pressure could have induced fluid precipitation at hydrostatic or at least sub–lithostatic conditions (as the primary FIA-BV1; e.g., Sibson, 1992). As progression of quartz development and fracture fill, pressure increased towards the lithostatic domain could have promoted sealing of fractures at higher pressures (as the secondary FIA-BV2). Thus, the changing pressure conditions suggested by fluid

inclusions and crack–and–seal vein textures might be related to fault valve behavior related to seismic pumping under greenschist metamorphic conditions (e.g., Sibson et al., 1975; Sibson, 1992). Although the ultimate fluid source for this stage is not well constrained, the low salinity fluids and timing relationships relative to metamorphism and deformation favor the interpretation that hydrothermal fluid was generated by prograde metamorphism of the siliciclastic–dominant pile.

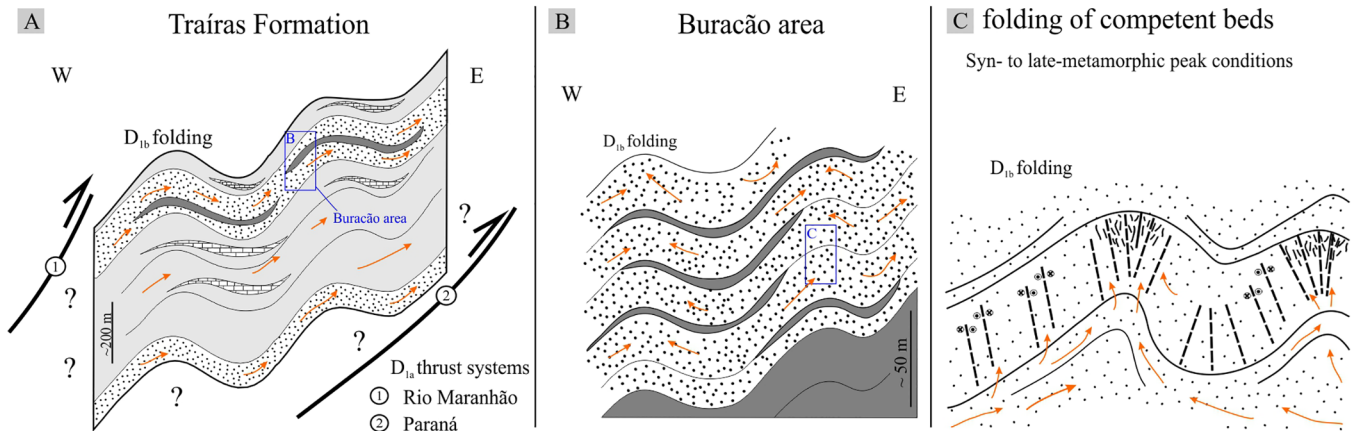### 5.2. The syn-D_{2a} type II ore–bearing veins and the pyritic ore precipitation

5.2.1. Pyritic ore precipitation: evidence from the mineral paragenesis

Textural associations between pyrite, gold–bearing arsenopyrite and free gold metal alloys (Figs. 4 and 6) constrain a domain of T–fS_2–fO_2 conditions for the pyritic ore precipitation. Equilibrium temperature for arsenopyrite inclusions in pyrite (arsenic content 28.8–30.4 at.% As; Fig. 10B) is estimated between 285 and 345 °C (cf. Kretschmar and Scott, 1976; Sharp et al., 1985). This range corresponds to fS_2 of $10^{-11.8}$–$10^{-8.4}$ for the pyrite host (cf. Sharp et al., 1985; Fig. 10B), with fO_2 lower than 10^{-29} in the Py–Asp fS_2–fO_2 stability field (cf. Holland, 1959; Fig. 10C). These temperature and fO_2 conditions for ore precipitation are lower than those estimated for the metamorphic peak (Fig. 10A). These estimations can be interpreted as consistent with a first syn–D_{1a} metamorphic peak buffered by an oxide–dominated assemblage in host phyllites (Mt ± Hm, Py), and a distinct, second syn–D_{2a} episode buffered by the pyritic ore precipitation along type II veins (Py, Po, Asp; Fig. 10C). Within the pyritic ore, the variability of mineral inclusions in pyrite from distal (Mt, Hm, Po) to proximal (Po, Cpy) alteration halos as well as in type II veins (Po, Cpy, Asp, Bsm, gold) suggest either (i) several sulfide precipitation episodes, or (ii) spatially–related fS_2–fO_2 fluctuations during a single episode of ore deposition. The broad occurrence of massive pyrite in the pyritic ore without overgrowth textures and mineralogical zonation favor the second possibility. In this sense, the distribution of mineral inclusions in the distal and proximal alteration halos could suggest a transition from Mt-Hm-Py stability in the host rocks towards Py-Po-Asp stability in the proximal halos and ore veins, i.e., the reduced fluid corridor. These
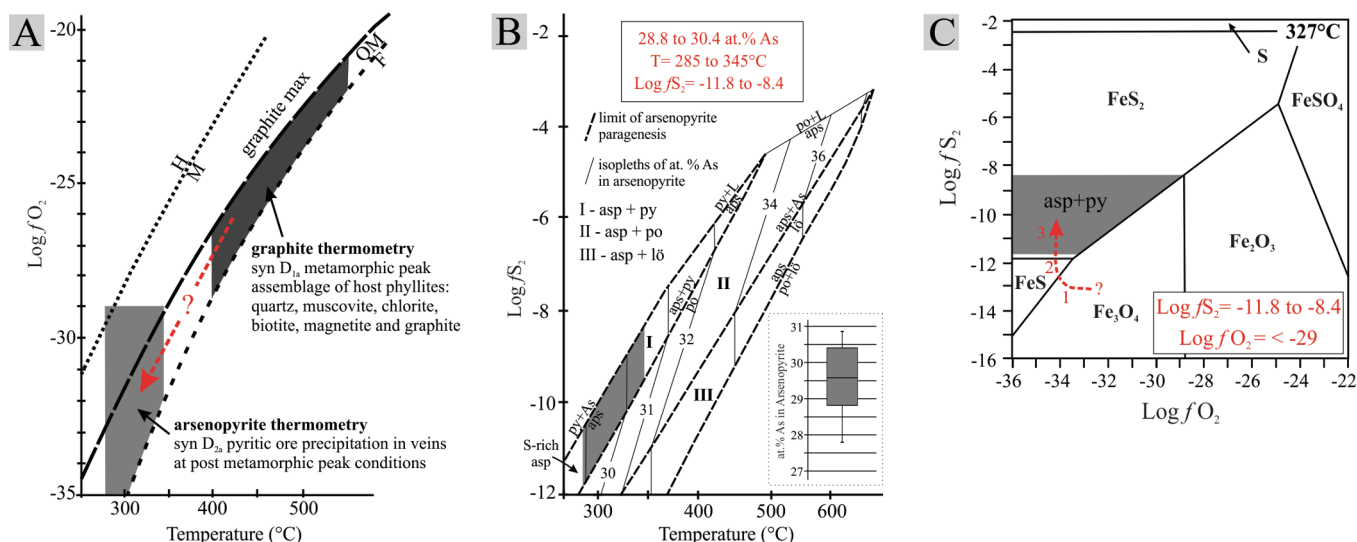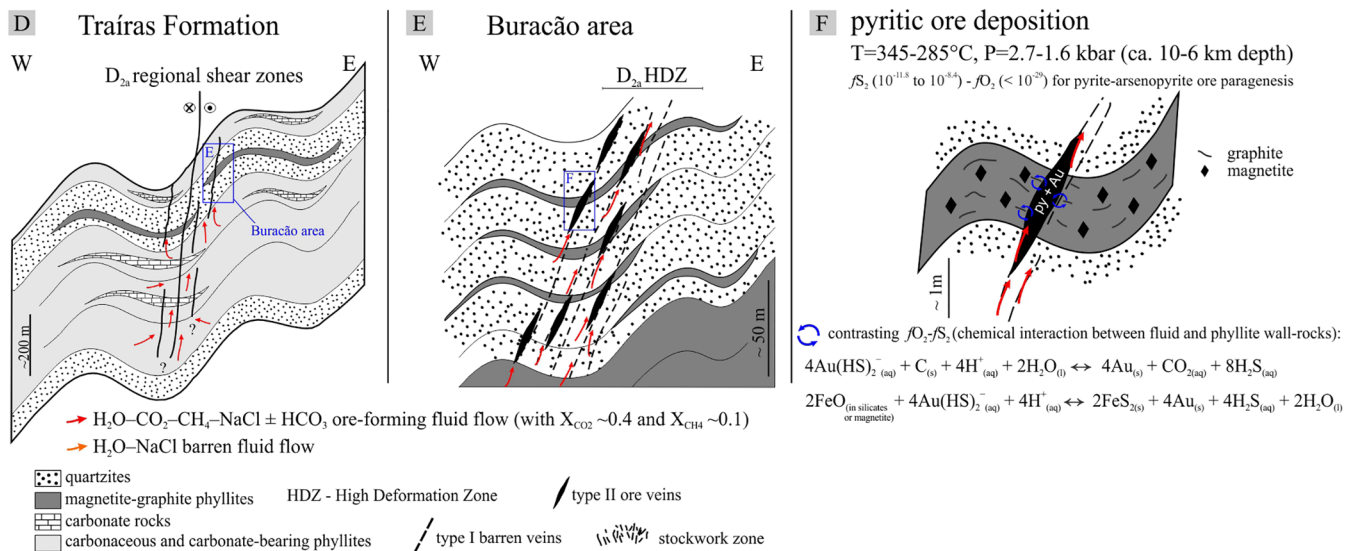

Fig. 10. Estimations of temperature and fO_2–fS_2 for the metamorphic peak condition and for the pyritic ore deposition. (A) Temperature vs. fO_2 expected for the metamorphic peak and the pyritic ore deposition based on the graphite and arsenopyrite thermometers (H: hematite, M: magnetite, QFM: quartz-fayalite-magnetite buffers; modified after Spear, 1993). (B) Estimation of temperature vs. fS_2 for the pyritic ore deposition based on the arsenopyrite–pyrite thermometry (cf. Sharp et al., 1985). (C) fO_2–fS_2 arsenopyrite–pyrite stability field (cf. Holland, 1959) showing fugacity fluctuations during the pyritic ore deposition, i.e., chemical interaction between ore–forming fluid and wall phyllites. The transformation of Mt (± Hm) from the host phyllites into Po (Py) at hydrothermal halos suggests an initial decreasing fO_2, which may be related to CH_4–producing reactions with the wall carbon–bearing phyllites. The influxes of sulfur–rich mineralizing fluids increase the fS_2 and drive the system from Mt (1) to Po (2) stability field via systematic conversion of Mt(Hm) into Po(Py). However, these conversions are incomplete in the distal hydrothermal halos, preserving oxide inclusions within the pyritic ore. In the proximal hydrothermal portions that correspond to the fluid input focusing corridor, and where mineralizing fluid influxes are higher, the system is driven towards the Py–Asp stability field (3) with Au (As, Bi, Ag) precipitation in veins (see Fig. 11F).

Type I barren veins

A — Traíras Formation
B — Buracão area
C — folding of competent beds

Type II ore veins

D — Traíras Formation
E — Buracão area
F — pyritic ore deposition

Fig. 11. Schematic metamorphic–hydrothermal model for the genesis of type I barren and type II ore–bearing veins, and the pyritic ore deposition in the Buracão area. *Type I barren veins*: (A) syn–D$_1$ metamorphic peak produces fluids that percolate along regional and local D$_{1a-b}$ sub–horizontal structures cross–cutting metasedimentary rocks. (B) In the Buracão area, the main D$_{1b}$ folding of competent quartzite layers produced conjugated shear and extensional fractures with stockwork zones, which represent sites to fluid flow and formation of type I barren veins through a seismic pump system (C). *Type II ore–bearing veins*: (D) metamorphic fluids with S-species, metals (including gold), and CO$_2$–CH$_4$ ± HCO$_3$ compounds are generated from carbonaceous phyllites and carbonate rocks of the Traíras formation. These ore–forming fluids percolate along 1st order regional D$_{2a}$ subvertical shear zones cross–cutting the Traíras Formation (intrabasinal scale) to 2nd or 3rd order structures at the Buracão area. (E) In the study area, these fluids are collected into minor shear fractures (dilatational zones) along HDZ, with formation of type II ore–bearing veins. (F) Then, the pyritic ore precipitation is induced by chemical interaction, i.e., contrasting fO$_2$–fS$_2$ between percolating ore–forming fluid and host magnetite–graphite phyllites, which acted as a lithological barrier (see Fig. 10C).

fS$_2$–fO$_2$ fluctuations were probably induced via interaction between the sulfidic fluid and the host phyllites, promoted by fractures cross–cutting the graphite–magnetite layers in the host rocks, which conditioned ore deposition (lithological barrier control).

5.2.2. Type II ore veins: P_t–T_t–X pathways and implications for ore genesis

The different types of primary fluid inclusions (FIAs OV1a, OV1b and OV1c) with different compositions (i.e., H$_2$O–CO$_2$–CH$_4$–NaCl ± HCO$_3$, locally halite ± calcite saturated) indicate a compositionally heterogeneous fluid system related to the ore–bearing veins. The FIAs OV1a and OV1c aqueous–carbonic fluids show different density (∼0.84 and 0.95–1.00 g/cc, respectively) and salinity (9.3–10.6 and 28.3–29.3 eq. wt% NaCl, respectively) for similar Th$_{tot}$ range (260–345 and 295–344 °C), while FIA-OV1b is carbonic (∼0.59 g/cc; Table 2). Coupled with the coexistence of CO$_2$–CH$_4$ (FIA-OV1b) and H$_2$O–CO$_2$–CH$_4$ (FIAs OV1a and OV1c), both with similar CO$_2$:CH$_4$ proportions in the carbonic phase, these features may suggest both (i)

interaction with different source–rocks, and/or (ii) fluid immiscibility due to pressure fluctuations during fracturing.

The first hypothesis is supported by the presence of different chemical components like CO$_2$–CH$_4$ as well as halite ± calcite daughter crystals. These may have been incorporated from multiple wall lithologies (e.g., Yardley and Graham, 2002), such as carbonaceous phyllites and carbonate–bearing rocks of the Traíras Formation. This hypothesis is consistent with the salinity increase from FIAs OV1a to OV1c that is accompanied by the occurrence of calcite daughter crystals. The feature is probably related to increasing calcite solubility in CO$_2$–bearing hydrothermal fluids leading to the increase in the fluid capability to dissolve and transport carbonatic compounds (cf. Yang et al., 2013). Indeed, in view of the absence of volcanic rocks in the region, and the large proportion of carbonic phases in FIs carbon must have originated from organic matter decomposition and/or carbonatic rocks devolatilization during metamorphism. Fluid mixing may have occurred in the precipitation sites, with the participation of local CH$_4$–CO$_2$ fluids

produced by hydrolysis of carbonaceous material in adjacent graphite–rich phyllites (e.g., Cox et al., 1995; Lobato et al., 2001). This would have increased fluid CH_4 content and decreased fO_2 conditions at the onset of ore formation, with production of carbonic FIA-OV1b in ore veins. This hypothesis implies that the quartz veins have trapped fluids of heterogeneous origin due to complex fluid pathways moving through the rock package (Fig. 11).

On the other hand, fluid immiscibility is supported by the coexistence of lower density carbonic fluid (FIA-OV1b) with higher density aqueous–carbonic fluids (FIAs OV1a and OV1c). All of them show similar CH_4:CO_2, and suggest exsolution between CO_2–CH_4 and H_2O–CO_2–CH_4 fluids, which may be related to CO_2 solubility in aqueous fluids. Fluid immiscibility could be related to pressure fluctuations produced in the fracture opening episode. These features are similar to those described in shear–related veins in orogenic gold deposits such as those in the Abitibi belt, Canada (e.g., Neumayr and Hagemann, 2002 and references therein).

The similar Py–Asp formation temperatures (285–345 °C) and fluid inclusions Th_{tot} (260–345 °C; FIAs OV1a and OV1c) suggest two hypotheses for the development of the ore–bearing veins: (i) quartz and pyritic ore formed from different fluid pulses, or (ii) that they formed at a similar temperature range indicating a single fluid pulse for both. For the first hypothesis, early quartz may have formed at a higher temperature ($> Th_{tot}$) than the pyritic ore, and considerable re–cracking and sulfide precipitation would be needed to achieve the pyritic volume in veins (~20 to 40%). However, the homogeneous textures of sulfides and quartz do not support this hypothesis. In view of these constrains, the second hypothesis must be considered, which allows the association of quartz and pyritic ore data. Therefore, coupling primary FI (OV1a and OV1c) with Py–Asp data, P–T conditions for the generation of metal-rich hydrous fluids are thus estimated at 285–345 °C and 1.6–2.7 kbar (Fig. 9C), which correspond to depths of 6–10 km using the lithostatic gradient (Fig. 9C and D).

5.2.3. Mineralizing fluids: inferences of metal source, gold transport and ore deposition

The enrichment of As, Bi, Pb, Cu, Te, Se and Ag in pyrite crystals from the pyritic ore is similar to chemical signature of arsenian pyrite from carbonaceous phyllites (e.g., Thomas et al., 2011; Gregory et al., 2015). This is consistent with flat NASC–like REE pattern suggesting a sedimentary source for those chemical elements in fluids (e.g., Rollinson, 1992; Fig. 5). However, the host phyllites with pyrite filling microboudins do not represent a suitable source rock, since they record, at their P–T maximum conditions, sulfide precipitation rather than dissolution. Also, this syn-D_{1a} pyrite precipitation is older than the syn-D_{2a} pyritic ore, ruling out clear genetic relationships between them. Moreover, the syn-D_{1a} sulfide paragenesis with abundant pyrite and absent pyrrhotite indicates that metamorphism did not apparently release metals to fluids by the pyrite–pyrrhotite conversion (cf. Large et al., 2011). A similar protolith metamorphosed to upper greenschist grade, for example rocks exposed in the north or west of the study area (Fuck and Marini, 1981; Tanizaki et al., 2015) could have been the source of metals for the ore–forming fluids, similarly to what is described for the Bendigo Gold Mine, Australia (Thomas et al., 2011) and gold deposits in Otago, New Zealand (Pitcairn et al., 2006). In this case, metal-rich fluids would have percolated along regional shear zones through the Traíras Formation (Fig. 11D) and subsequently channelized along D_{2a} structures towards the Buracão area under post–metamorphic peak conditions (Fig. 11E).

The gold occurrences as high fineness (> 800) metal alloys, accompanied by As, Bi and Ag within pyrite–arsenopyrite–bismuthinite association in the pyritic ore, lead us to classify the study area as "a gold-only orogenic ore deposit", typically found in low–grade metamorphic terrains (e.g., Morrison et al., 1991; Phillips and Powell, 2015). The presence of reduced C–O–H–S fluids in this low–grade metamorphic environment suggests that the metal transport was primarily via $Au(HS)_2^-$ complexes (Pal'yanova, 2008; Williams-Jones et al., 2009) with minor influence of $Ag(HS)_2^-$ and Bi–bisulfides species such as $Bi_2S_2(OH)_2^0$ or

$HBi_2S_4^-$ (cf. Skirrow and Walshe, 2002). The ubiquitous occurrence of bismuth with gold suggests a process of Au scavenging by Bi in the fluid, which contributed to increasing fineness of the precipitated gold particles (e.g., Tooth et al., 2008 and references therein). Similarly, the close association between Au and As suggests a chemical affinity between both elements (e.g., Deditius et al., 2014), where arsenic played an important role to concentrate structural gold within sulfides.

Based on the occurrence of type II ore–bearing veins always cross–cutting graphite–magnetite phyllites, we suggest that gold precipitation was induced by the interaction between aqueous, Au–bisulfide complexes and graphite in host rocks (Eq. (1): $4Au(HS)_{2(aq)}^- + C_{(s)} + 4H_{(aq)}^+ + 2H_2O_{(l)} \leftrightarrow 4Au_{(s)} + CO_{2(aq)} + 8H_2S_{(aq)}$; e.g., Cox et al., 1995; Bierlein and Maher, 2001). In addition, the abundant iron–rich minerals in these phyllites must have favored gold precipitation through sulfidation (Eq. (2): $2FeO_{(in\ silicates\ or\ magnetite)} + 4Au(HS)_{2(aq)}^- + 4H_{(aq)}^+ \leftrightarrow 2FeS_{2(s)} + 4Au_{(s)} + 4H_2S_{(aq)} + 2H_2O_{(l)}$; Fig. 11F). These equations highlight the pyrite–gold association in the pyritic ore, and are consistent with the sulfide–oxide textures, linking small fO_2–fS_2 fluctuations and gold precipitation. In this scenario, graphite and iron–rich minerals in host rocks would reduce gold or decrease sulfur content in solution, respectively, destabilizing Au–bisulfides and inducing gold precipitation. Therefore, the occurrence of type II ore–bearing veins and the spatial distribution of the mineralization point out the participation of the host magnetite–graphite phyllites as lithological controls and chemical barriers, i.e., fO_2–fS_2 buffers, for ore deposition in the Buracão area.

6. Conclusions

The mineralogical, geochemical and fluid inclusion data presented here allow us to link metamorphism and deformation of the metasedimentary Traíras Formation to generate the orogenic gold mineralization in the Buracão area via a metamorphic–hydrothermal model. The study area evolved through the syn–D_{1a} metamorphic peak (i.e., 400–560 °C and < 6 kbar; shallower than 17 km depth), followed by a syn–D_{1b} barren type I vein generation during the syn– to late–metamorphic peak stage. Later, the syn–D_{2a} ore–bearing type II veins and gold mineralization occurred under post–metamorphic peak conditions (i.e., 285–345 °C and 1.6–2.7 kbar; 6–10 km depth).

We interpret that the precipitation of quartz and pyritic ore with Au (As, Bi, Ag) in type II veins from H_2O–CO_2–CH_4–NaCl $\pm$ HCO_3 mineralizing fluids was induced by contrasting fO_2–fS_2 related to fluid:rock interaction. In this case, the host phyllites (graphite and magnetite–dominant Fe–O $\pm$ S, Cu, Zn system) have acted to chemically control ore deposition (pyrite–dominant Fe–S $\pm$ As, Bi, Cu system) with participation of graphite and CO_2–CH_4 contribution to the fluid. The ultimate metal source appears to be external to the immediate metasedimentary rock succession, because early sulfides, particularly pyrite, are preserved in the local host phyllites. However, the chemistry of the fluid inclusions and inferred metal precipitation process is most consistent with mixing of local volatiles in the host rocks with metals and sulfur derived from other parts of the metasedimentary pile. In this sense, a stable isotope study (O, H, C, and S) would be the first focus on a regional study to identify fluids related to regional metamorphism, and tackle other questions not addressed in this paper such as the ultimate source of sulfur and fluid compounds.

Important exploration implications must be taken into account once the Buracão area is identified as an orogenic gold deposit. The set of structures, the P–T–X fluid conditions and ore genesis, the timing between metamorphic peak and mineralization, as well as the host lithologies place the area in the general context of other orogenic gold deposits at the external domain of the Neoproterozoic Brasilia Fold Belt (BFB) such as Luziânia, Santa Rita and the world-class Morro do Ouro–Paracatu deposits (e.g., Hagemann et al., 1992; Giuliani et al., 1993; Oliver et al., 2015). All of these deposits are hosted in Paleo– to Neoproterozoic low–grade metamorphic metasedimentary successions, metamorphosed near synchronously during the Neoproterozoic

Brasiliano Orogeny (e.g., Pimentel, 2016), with no evidence of related magmatism. The results presented here highlight the potential of Precambrian metasedimentary piles, even those that do not show intercalations with metavolcanic rocks, to generate orogenic gold deposits through the hydrothermal–metamorphic model. The model seems to be applicable for many deposits in the external domain of the BFB and for other metasedimentary–hosted deposits globally, and expands the geological setting for exploration of this gold mineralization type.
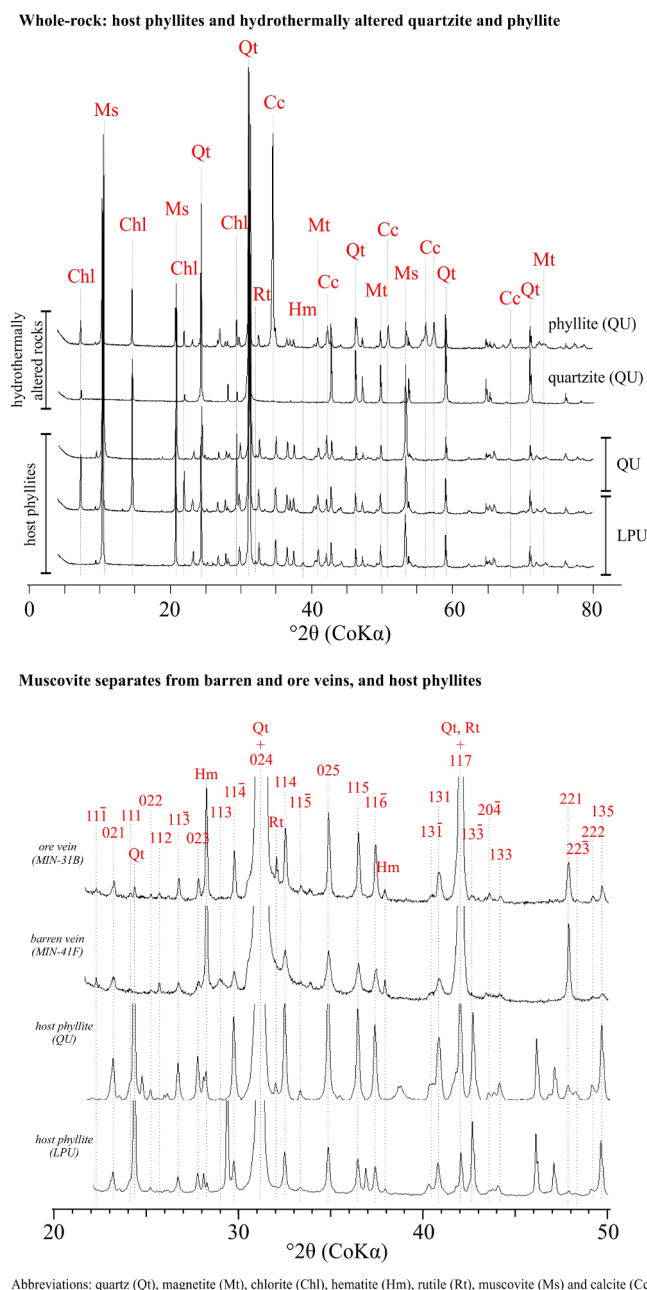
Acknowledgments

Appendix

Appendix 1, 2 and 4 and Appendix 3.

Appendix 1. Representative X–ray powder diffraction patterns of whole–rocks and muscovite separates.

Carbonaceous material in phyllites

Variable density of CO_2–CH_4 compounds in aqueous-carbonic fluid inclusions (FI)

Rhombohedral shape daughter mineral in halite–saturated FI
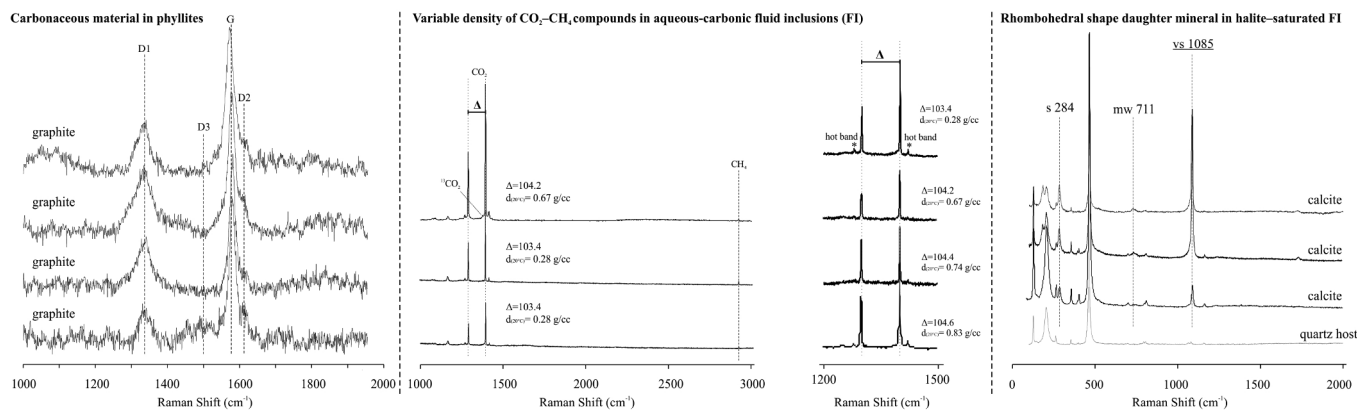
Graphite geothermometer data

Analysis	Position			FWHM			Height			Area			R1	R2	T(°C)
	D1	G	D2	D1	G	D2	D1	G	D2	D1	G	D2			
G1	1334.16	1573.32	1609.64	24.44	21.01	28.27	223.64	607.09	90.10	8587.03	20032.00	4001.19	0.37	0.26	524
G2	1331.15	1576.03	1611.01	44.92	15.52	31.01	167.32	315.99	73.68	11806.30	7701.84	3589.11	0.53	0.51	414
G3	1334.63	1578.02	1611.29	45.87	19.97	15.75	119.24	256.15	47.03	8591.60	8035.52	1163.87	0.47	0.48	426
G4	1336.08	1579.48	1611.75	43.01	19.21	17.80	128.09	229.39	38.28	8653.24	6922.09	1070.19	0.56	0.52	410
G5	1333.64	1581.23	1614.92	49.34	12.48	13.81	89.88	262.02	28.62	6966.58	5135.66	620.62	0.34	0.55	400
G6	1337.27	1580.35	1617.34	19.14	20.93	14.02	57.99	214.15	34.27	1742.93	7040.24	754.83	0.27	0.18	560

Appendix 2. Representative Raman spectra of carbonaceous material in phyllites and fluid compounds in FI from type II veins.

Appendix 3
Chemical composition of sulfides and muscovite.

Chemical composition of sulfides from host phyllites

CHALCOPYRITE						SPHALERITE			PYRITE				
wt.% (SEM-EDS)			$Cu_{0.8-1.0}Fe_{1.0-1.2}S_2$			$(Zn_{0.8-1.0}, Fe_{0.0-0.2})S$			$Fe_{1.0-1.2}S_2$				
Cu	35.1	33.2	27.4	37.4	35.7	3.7	b.d.l.	b.d.l.	b.d.l.	b.d.l.	0.7	b.d.l.	b.d.l.
Zn	0.3	b.d.l.	b.d.l.	0.4	b.d.l.	54.7	62.2	58.3	1.1	b.d.l.	1.0	b.d.l.	b.d.l.
Fe	33.3	30.9	33.5	33.0	32.4	8.8	b.d.l.	0.9	49.1	49.2	45.1	51.6	44.4
S	30.8	34.4	31.6	30.8	26.1	30.0	30.0	36.7	43.4	45.2	48.4	45.7	45.1
Bi	2.2	1.9	1.4	1.9	1.9	1.9	1.7	3.7	3.3	4.4	2.7	2.5	2.3
As	0.5	0.7	b.d.l.	0.5	0.6	0.9	b.d.l.	b.d.l.	b.d.l.	1.2	0.6	b.d.l.	b.d.l.
Total	102.3	101.1	94.0	104.0	96.7	100.0	94.0	99.7	97.0	100.0	98.4	99.8	91.8

Chemical composition of muscovite and sulfides from veins

MUSCOVITE				PYRRHOTITE		PYRITE						
Sample	MIN-41F	MIN-85A	MIN-31C	Sample	MIN-24B	MIN-24B	MIN-206A	MIN-41C	MIN-19C	MIN-01A	MIN-31C
ppm (ICP-MS)	type I	type II	type II	type II (α)	(α)	(α)	(α)	(β)	(β)	(β)	
La	0.045	0.015	0.05	wt. % (XRF)							
Ce	0.453	0.036	0.14	Fe	49.9	51.8			56.7		
Pr	0.009	0.004	0.018	S	49.4	47.7			42.2		
Nd	0.033	0.018	0.071	LOI	b.d.l.	b.d.l.			b.d.l.		
Sm	0.006	0.008	0.024	Total	99.3	99.5			98.9		
Eu	0.008	0.059	0.032	wt.% (SEM-EDS)							
Gd	0.02	0.04	0.041	Au	n.a.	n.a.	n.a.	n.a.	n.a.	up to 0.4	up to 0.5
Tb	0.001	0.006	0.01	ppb (ICP-MS)							
Dy	0.003	0.056	0.08	Te	376.1	1.35	0.27	49.4	2536.5	170.15	1463.9
Ho	0.001	0.019	0.023	Pd	b.d.l.	0.95	0.94	3.5	b.d.l.	1.42	3.0
Er	0.003	0.072	0.075	Pt	b.d.l.	b.d.l.	b.d.l.	b.d.l.	b.d.l.	0.05	b.d.l.
Tm	0.001	0.017	0.016	ppm (ICP-MS)							
Yb	0.003	0.123	0.1	As	5004.56	1599.7			11140.73	3203.30	
Lu	0.002	0.108	0.08	Bi	312.19	95.9			31667.15		
Y	0.016	0.374	0.387	Cu	719.7	545.31			930.94	216.81	
Eu/Eu*	10	16.67	10	Zn	27.29	20.59			23.78	239.74	
La_N/Yb_N	b.d.l.	0.001	0.001	Ag	1.79	2.15			50.11	0.52	
ΣREE	0.59	0.58	0.76	Pb	187.07	171.41			17677.65	165.84	
ARSENOPYRITE				Se	38.13	28.6			185.68		
wt.% (SEM-EDS)			$Fe_{1.0}As_{0.8-0.9}S_{1.1-1.3}$	Cr	6.97	5.78			3.94		
As	Fe	S	Au	Co	190.65	31.84			133.54		
					total	As at.%					
41.1	33.9	24.3	0.8	100.0	28.7	Ni	144.18	96.29			90.68	
42.4	34.8	21.7	0.9	99.9	30.3	S/Se	12,955	16,678			2273	

Appendix 3 (*continued*)

Chemical composition of sulfides from host phyllites													
40.9	34.7	23.4	0.9	100.0	28.8	La	0.066	6.66	65.175	0.004	0.044	19.855	0.003
39.9	34.0	24.9	1.2	99.9	27.8	Ce	0.173	14.883	73.652	0.03	0.259	39.968	0.009
40.5	33.8	25.2	0.5	100.0	27.9	Pr	0.017	1.504	0.131	b.d.l.	0.013	4.43	b.d.l.
41.2	37.1	23.7	n.a.	102.0	28.1	Nd	0.085	5.209	0.49	0.002	0.048	15.855	b.d.l.
40.7	35.9	22.9	n.a.	99.4	28.6	Sm	0.012	0.831	0.083	b.d.l.	0.011	3.123	b.d.l.
42.5	37.5	23.3	n.a.	103.3	28.9	Eu	0.003	0.138	0.017	b.d.l.	0.004	0.545	b.d.l.
41.1	36.2	22.2	n.a.	99.5	29.0	Gd	0.009	0.754	0.529	b.d.l.	0.011	3.062	b.d.l.
42.0	35.1	23.1	n.a.	100.2	29.4	Tb	0.001	0.073	0.024	b.d.l.	0.002	0.344	b.d.l.
41.8	36.1	21.9	n.a.	99.8	29.5	Dy	0.001	0.189	0.083	b.d.l.	b.d.l.	1.054	b.d.l.
41.7	37.2	21.0	n.a.	100.0	29.6	Ho	0.001	0.028	0.021	b.d.l.	0.001	0.155	b.d.l.
43.4	37.5	21.7	n.a.	102.6	30.1	Er	0.006	0.088	0.07	b.d.l.	0.004	0.396	b.d.l.
42.3	37.7	20.3	n.a.	100.3	30.1	Tm	b.d.l.	0.012	0.014	b.d.l.	0.001	0.049	b.d.l.
41.5	36.3	19.7	n.a.	97.5	30.4	Yb	0.005	0.074	0.091	b.d.l.	0.001	0.273	b.d.l.
43.4	36.0	21.5	n.a.	100.9	30.5	Lu	0.001	0.021	0.024	b.d.l.	0.001	0.06	b.d.l.
42.1	34.1	21.1	n.a.	97.3	30.7	Y	0.089	0.339	0.467	0.014	0.06	2.874	0.014
42.5	34.1	21.2	n.a.	97.8	30.8	Eu/Eu*	b.d.l.	0.78	0.32	b.d.l.	b.d.l.	0.79	b.d.l.
44.3	36.7	21.4	n.a.	102.4	30.9	La$_N$/Yb$_N$	b.d.l.	10.5	70	b.d.l.	b.d.l.	7.11	b.d.l.
						ΣREE	0.38	30.46	140.41	0.04	0.4	89.17	0.01

b.d.l. = below detection limit; n.a. = not analysed; type I = barren veins, type II = ore-bearing veins.
(α) pyrite in association with pyrrhotite and magnetite; (β) pyrite in association with arsenopyrite and bismuthinite.
REE normalized to the NASC composition (Gromet et al., 1984).
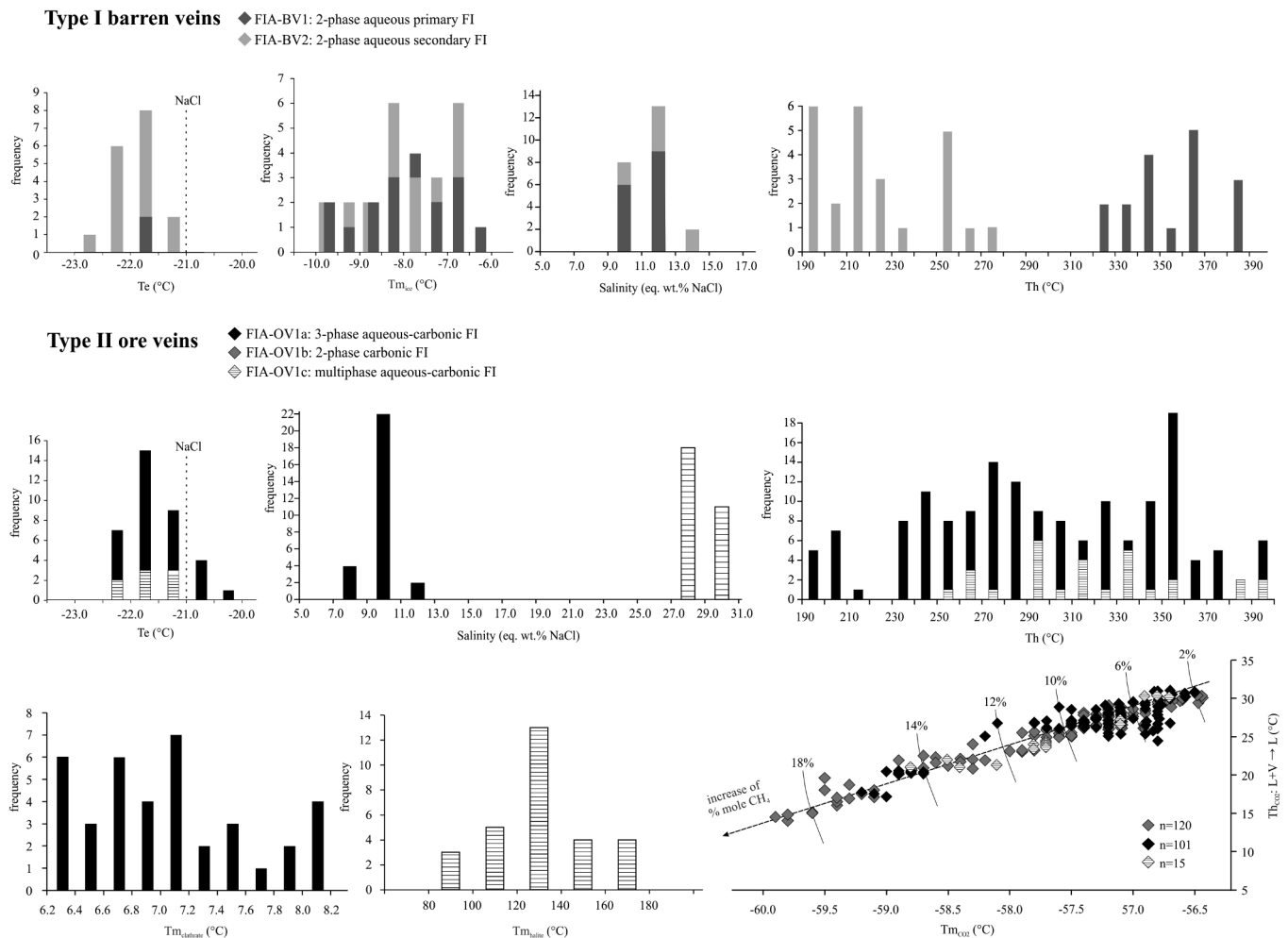
Appendix 4. Microthermometric measurements in fluid inclusions from barren and ore veins.

Appendix A. Supplementary data

Supplementary data to this article can be found online at https://doi.org/10.1016/j.oregeorev.2018.12.017.

References

Bakker, R.J., 2003. Package FLUIDS 1. Computer programs for analysis of fluid inclusion data and for modelling bulk fluid properties. Chem. Geol. 194, 3–23.

Best, M.G., 2003. In: Igneous and Metamorphic Petrology, second ed. Blackwell Publishing, Malden, pp. 758.

Beyssac, O., Goffé, B., Chopin, C., Rouzaud, J.N., 2002. Raman spectra of carbonaceous material in metasediments: a new geothermometer. J. Metamorph. Geol. 20 (9), 859–871.

Bierlein, F.P., Maher, S., 2001. Orogenic disseminated gold in phanerozoic fold belts –examples from Victoria, Australia and elsewhere. Ore Geol. Rev. 18, 113–148.

Bodnar, R.J., 1993. Revised equation and table for determining the freezing point depression of H_2O–NaCl solutions. Geochim. Cosmochim. Acta 57, 683–684.

Bodnar, R.J., 2003. Introduction to aqueous fluid systems. In: In: Samson, I., Anderson, A., Marshall, D. (Eds.), Fluid Inclusions: Analysis and Interpretation 32. Mineral. Assoc. Canada, Short Course, pp. 81–99.

Cox, S., Sun, S., Etheridge, M., Wall, V., Potter, T., 1995. Structural and geochemical controls on the development of turbidite-hosted gold quartz vein deposits, Wattle Gully mine, central Victoria, Australia. Econ. Geol. 90, 1722–1746.

Dardenne, M.A., 2000. The Brasília fold belt. In: Cordani, U.G., Milani, E.J., Thomaz, Filho A., Campos, D.A. (Eds.), Tectonic Evolution of South America. 31st International Geological Congress, Rio de Janeiro, pp. 231–236.

Dardenne, M.A., Botelho, N.F., 2014. Metalogênese da Zona Externa da Faixa Brasília. In: Silva, M.G., Rocha Neto, M.T., Jost, H., Kuyunjian, R.M. (Eds.), Metalogênese das Províncias Tetônicas Brasileiras-Programa Geologia do Brasil/Recursos Minerais/ Série Metalogenia. CPRM, Belo Horizonte, pp. 431–452.

Deditius, A.P., Reich, M., Kesler, S.E., Utsunomiya, S., Chryssoulis, S.L., Walshe, J., Ewing, R.C., 2014. The coupled geochemistry of Au and As in pyrite from hydrothermal ore deposits. Geochim. Cosmochim. Acta 140, 644–670.

Doublier, M.P., Thebaud, N., Wingate, M.T.D., Romano, S.S., Kirkland, C.L., Gessner, K., Mole, D.R., Evans, N., 2014. Structure and timing of Neoarchean gold mineralization in the Southern Cross district (Yilgarn craton, Western Australia) suggest leading role of late low-Ca I-type granite intrusions. J. Struct. Geol. 67, 205–221.

Duan, Z., Møller, N., Weare, J.H., 1992a. An equation of state for the CH_4–CO_2–H_2O system: I. Pure systems from 0 to 1000 °C and 0 to 8000 bar. Geochim. Cosmochim. Acta 56, 2605–2617.

Duan, Z., Møller, N., Weare, J.H., 1992b. An equation of state for the CH_4–CO_2–H_2O system: II. Mixtures from 50 to 1000 °C and 0 to 1000 bar. Geochim. Cosmochim. Acta 56, 2619–2631.

Evans, K.A., Phillips, G.N., Powell, R., 2006. Rock-buffering of auriferous fluids in altered rocks associated with the Golden Mile-style mineralization, Kalgoorlie gold field, Western Australia. Econ. Geol. 101, 805–817.

Fuck, R.A., Marini, O.J., 1981. O Grupo Araxá e unidades homotaxiais. In: Symposium about São Francisco craton and their marginal belts, Salvador, 1, p. 118e130.

Giuliani, G., Olivo, G.R., Marini, O.J., Michel, D., 1993. The Santa Rita gold deposit in the Proterozoic Paranoá Group, Goiás, Brazil: an example of fluid mixing during ore deposition. Ore Geol. Rev. 8, 503–523.

Goldfarb, R.J., Baker, T., Dubé, B., Groves, D.I., Hart, C.J.R., Gosselin, P., 2005. Distribution, character, and genesis of gold deposits in metamorphic terranes. Econ. Geol. 407–450.

Goldfarb, R.J., Groves, D.I., 2015. Orogenic gold: Common or evolving fluid and metal sources through time. Lithos 233, 2–26.

Goldstein, R.H., Reynolds, T.J., 1994. . Systematic of Fluid Inclusions in Diagenetic Minerals 31, 198.

Gregory, D.D., Large, R.R., Halpin, J.A., Lounejeva Baturina, E., Lyons, T.W., Wu, S., Sack, P.J., Chappaz, A., Maslennikov, V.V., Bull, S.W., Danyushevsky, L., 2015. Trace element content of sedimentary pyrite in black shales. Econ. Geol. 110, 1389–1410.

Gromet, L.P., Dymek, R.F., Korotev, R.L., Haskin, L.A., 1984. The "North American shale composite": its compilation, major and trace element characteristics. Geochim. Cosmochim. Acta 48, 2469–2482.

Groves, D.I., Goldfarb, R.J., Gebre-Mariam, M., Hagemann, S.G., Robert, F., 1998. Orogenic gold deposits – a proposed classification in the context of their crustal distribution and relationship to other gold deposit types. Ore Geol. Rev. 13, 7–27.

Haar, L., Gallagher, J.S., Kell, G.S., 1984. NBS/NRC Steam Tables.

Hagemann, S.G., Brown, P.E., Walde, D.H.G., 1992. Thin-skinned thrust mineralization in the Brasilia fold belt: the example of the old Luziânia gold deposit. Miner. Deposita 27, 293–303.

Heyen, G., Ramboz, C., Dubessy, J., 1982. Simulation des equilibres de phases dans le systheme CO_2-CH_4 en dessous de 50°C et 100 bar. Application aux inclusions fluides. C. R. Acad. Sci. Paris 294, 203–206.

Holland, H.D., 1959. Some applications of thermochemical data to problems of ore deposits. I. Stability relations among the oxides, sulfides, sulfates and carbonates of ore and gangue metals. Econ. Geol. 54, 184–233.

Kretschmar, U., Scott, S.D., 1976. Phase relations involving arsenopyrite in the system Fe-As-S and their application. Can. Mineral. 14, 364–386.

Large, R.R., Bull, S.W., Maslennikov, V.V., 2011. A carbonaceous sedimentary source-rock model for Carlin-type and orogenic gold deposits. Econ. Geol. 106, 331–358.

Lobato, L.M., Ribeiro-Rodrigues, L.C., Vieira, F.W.R.V., 2001. Brazil's premier gold province. Part II: geology and genesis of gold deposits in the Archean Rio das Velhas greenstone belt, Quadrilátero Ferrífero. Mineral. Deposita 36, 249–277.

Lünsdorf, N.K., Dunkl, I., Schmidt, B.C., Rantitsch, G., Eynatten, H.V., 2013. Towards a higher comparability of geothermometric data obtained by Raman spectroscopy of carbonaceous material. Part I: evaluation of biasing factors. Geostand. Geoanal. Res. 38 (1), 73–94.

Morrison, G.W., Rose, W.J., Jaireth, S., 1991. Geological and geochemical controls on the silver content (fineness) of gold in gold-silver deposits. Ore Geol. Rev. 6, 333–364.

Neumayr, P., Hagemann, S.G., 2002. Hydrothermal fluid evolution within the Cadillac Tectonic Zone, Abitibi Greenstone Belt, Canada: Relationship to Auriferous Fluids in Adjacent Second- and Third-Order Shear Zones. Econ. Geol. 97, 1203–1225.

Oliver, N.H.S., Thompson, B., Freitas-Silva, F.H., Holcombe, R.J., Rusk, B., Almeida, B.S., Faure, K., Davidson, G.R., Esper, E.L., Guimarães, P.J., Dardenne, M.A., 2015. Local and regional mass transfer during thrusting, Veining, and Boudinage in the genesis of the Giant Shale-Hosted Paracatu Gold Deposit, Minas Gerais, Brazil. Econ. Geol. 110, 1803–1834.

Pal'yanova, G., 2008. Physicochemical modeling of the coupled behavior of gold and silver in hydrothermal processes: Gold fineness, Au/Ag ratios and their possible implications. Geochem. Geol. 255, 399–413.

Paringa Resources, 2012. http://www.paringaresources.com/brazil-gold–graphite-projects.html (accessed 16.03.17).

Phillips, G.N., Powell, R., 1993. Link between gold provinces. Econ. Geol. 88, 1084–1098.

Phillips, G.N., Powell, R., 2010. Formation of gold deposits – a metamorphic devolatilization model. J. Metamorph. Geol. 28, 689–718.

Phillips, G.N., Powell, R., 2015. A practical classification of gold deposits, with a theoretical basis. Ore Geol. Rev. 65, 568–573.

Pimentel, M.M., 2016. The tectonic evolution of the Neoproterozoic Brasília Belt, central Brazil: a geochronological and isotopic approach. Braz. J. Geol. 46 (1), 7–82.

Pimentel, M.M., Heaman, L., Fuck, R.A., Marini, O.J., 1991. U-Pb zircon geochronology of Precambrian tin-bearing continental-type acid magmatism in central Brazil. Precambrian Res. 52, 321–335.

Pimentel, M.M., Fuck, R.A., Jost, H., Ferreira Filho, C.F., Araújo, S.M., 2000. The basement of the Brasília Fold Belt and the Goiás Magmatic Arc. In: Cordani, U.G., Milani, E.J., Thomaz, Filho A., Campos, D.A. (Eds.), Tectonic Evolution of South America. 31st International Geological Congress, Rio de Janeiro, pp. 195–229.

Pires, G.L.C., Bongiolo, E.M., Renac, C., Nascimento, D.B., Prado, M., 2016. Structural and lithological controls of gold-bearing veins associated with the Brasiliano-Pan African Orogeny: an example from the Buracão Area, Araí Group (Brasília Fold Belt, Brazil). J. S. Am. Earth Sci. 66, 180–195.

Pitcairn, I.K., Teagle, D.A.H., Craw, D., Olivo, G.R., Kerrich, R., Brewer, T.S., 2006. Sources of metals and fluids in Orogenic Gold Deposits: insights from the Otago and Alpine Schists, New Zealand. Econ. Geol. 101, 1525–1546.

Reed, M.H., 1997. Hydrotermal alteration and its relationship to ore fluid composition. In: Barnes, H.L. (Ed.), Geochemistry of Ore Deposits, third ed. Jonh Wiley & Sons Inc, New York, pp. 303–365.

Renac, C., Kyser, K., Bowden, P., Moine, B., Cottin, J.-Y., 2010. Hydrothermal fluid interaction in basaltic lava units, Kerguelen Archipelago (SW Indian Ocean). Eur. J. Mineral. 22, 215–234.

Rollinson, H.R. (Ed.), 1992. Using Geochemical Data: Evaluation, Presentation, Interpretation. Longman Scientific & Technical, Michigan, pp. 352.

Sharp, Z.D., Essene, E.J., Kelly, W.C., 1985. A re-examination of the arsenopyrite geothermometer: pressure considerations and applications to natural assemblages. Can. Mineral. 23, 517–534.

Sibson, R.H., 1992. Fault-valve behavior and the hydrostatic-lithostatic fluid pressure interface. Earth Sci. Rev. 32, 141–144.

Sibson, R.H., Moore, J., Rankin, A.H., 1975. Seismic pumping – a hydrothermal fluid transport mechanism. J. Geol. Soc. (London) 131, 653–659.

Skirrow, R.G., Walshe, J.L., 2002. Reduced and oxidized Au-Cu-Bi iron oxide deposits of the Tennant Creek Inlier, Australia: an integrated geologic and chemical model. Econ. Geol. 97, 1167–1202.

Spear, F.S., 1993. Metamorphic phase equilibria and pressure–temperature–time paths. Mineral. Soc. Am. Monogr. (1), 799.

Steele-MacInnis, M., Lecumberri-Sanchez, P., Bodnar, R.J., 2012. HOKIEFLINCS_H2O-NACL: a Microsoft Excel spreadsheet for interpreting microthermometric data from fluid inclusions based on the PVTX properties of H_2O–NaCl. Comput. Geosci. 49, 334–337.

Tanizaki, M.L.N., Campos, J.E.G., Dardenne, M.A., 2015. Estratigrafia do Grupo Araí: registro de rifteamento paleoproterozoico no Brasil Central. Braz. J. Geol. 45 (1), 95–108.

Thiery, R., Vidal, J., Dubessy, J., 1994. Phase equilibria modeling applied to fluid inclusions: liquid– vapour equilibria and calculation of the molar volume in the CO_2–CH_4–N_2 system. Geochim. Cosmochim. Acta 58, 1073–1082.

Thomas, H.V., Large, R.R., Bull, S.W., Maslennikov, V.V., Berry, R.F., Fraser, R., Froud, S., Moye, R., 2011. Pyrite and pyrrhotite textures and composition in sediments, laminated quartz veins, and reefs at Bendigo gold mine, Australia: insights for ore genesis. Econ. Geol. 106, 1–31.

Tomkins, A.G., 2013. On the source of orogenic gold. Geology 41 (12), 1255–1256.

Tooth, B., Brugger, J., Ciobanu, C., Liu, W., 2008. Modeling of gold scavenging by bismuth melts coexisting with hydrothermal fluids. Geology 36, 815–818.

Yang, K., Heo, S., Hwang, J., Park, S.G., Koh, S., 2013. Calcite-saturated fluids trapped in fluorite from the Gagok Zn-Pb skarn deposit, South Korea. Can. Mineral. 51, 613–628.

Yardley, B.W.D., Graham, J.T., 2002. The origins of salinity in metamorphic fluids. Geofluids 2, 249–256.

Wang, X., Chou, I.M., Hu, W., Burruss, R.C., Sun, Q., Song, Y., 2011. Raman spectroscopic measurements of CO_2 density: experimental calibration with high-pressure optical cell (HPOC) and fused silica capillary capsule (FSCC) with application to fluid inclusion observations. Geochim. Cosmochim. Acta 75, 4080–4093.

Williams-Jones, A.E., Bowell, R.J., Migdisov, A.A., 2009. Gold in solution. Elements 5, 281–287.

Zhang, Y.G., Frantz, J.D., 1987. Determination of the homogenization temperatures and densities of supercritical fluids in the system $NaCl–KCl–CaCl_2–H_2O$ using synthetic fluid inclusions. Chem. Geol. 64, 335–350.

Zviagina, B.B., Skharov, B.A., Drits, V.A., 2007. X-ray diffraction criteria for the identification of *trans-* and *cis-*vacant varieties of dioctahedral micas. Clays Clay Miner. 55 (5), 467–480.